applied sciences

MDPI

Article

EM Scattering of A Target above Canyon/Valley Environment Based on Composite Rough Surface Modeling Method and Modified SBR-FBSSA Algorithm

Yijin Wang [1], Chuangming Tong [1], Tong Wang [1,*], Ximin Li [2,*], Qingkuan Wang [1] and Zhaolong Wang [1]

[1] Air Defense and Missile Defense College, Air Force Engineering University, Xi'an 710051, China; wang_cem@163.com (Y.W.)
[2] National Key Laboratory of Radar Signal Processing, Xidian University, Xi'an 710071, China
* Correspondence: tongw08@163.com (T.W.); xmli@xidian.edu.cn (X.L.)

Featured Application: The method proposed can be used for canyon/valley environment modeling and electromagnetic scattering characteristics analysis for targets and composite environments.

Abstract: The composite electromagnetic (EM) scattering characteristics from a target above a canyon/valley environment are significant. Aiming to acquire the composite EM scattering efficiently and accurately, the framework of the canyon/valley environment modeling method and modified shooting and bouncing rays (SBR) hybrid with facet-based small slope approximation (FBSSA) algorithm is investigated. Firstly, the canyon/valley environment containing two slopes and a bottom modeling method is proposed. Then, considering the environment's roughness, the modified SBR algorithm introduced by the high-order reflection model is proposed. Combined with the FBSSA, the modified SBR-FBSSA algorithm is an efficient and accurate method to predict composite EM scattering based on numerical verification. Finally, the effects of different surface types, roughness, slope angles, and incident-pitch and azimuth angles on the composite EM scattering characteristics are further analyzed. The work presented in this article provides a way to study the composite EM scattering from a target above the canyon/valley environment. Meanwhile, the complex scattering mechanism is revealed, and some valuable conclusions are put forward based on the physical phenomena.

Keywords: canyon/valley environment modeling; modified shooting and bouncing rays; high-order reflection model; facet-based small slope approximation; composite electromagnetic scattering

check for updates

Citation: Wang, Y.; Tong, C.; Wang, T.; Li, X.; Wang, Q.; Wang, Z. EM Scattering of A Target above Canyon/Valley Environment Based on Composite Rough Surface Modeling Method and Modified SBR-FBSSA Algorithm. *Appl. Sci.* **2023**, *13*, 4427. https://doi.org/10.3390/app13074427

Academic Editor: Ernesto Limiti

Received: 23 February 2023
Revised: 28 March 2023
Accepted: 28 March 2023
Published: 30 March 2023

Copyright: © 2023 by the authors. Licensee MDPI, Basel, Switzerland. This article is an open access article distributed under the terms and conditions of the Creative Commons Attribution (CC BY) license (https://creativecommons.org/licenses/by/4.0/).

1. Introduction

The composite electromagnetic (EM) scattering characteristics of targets above random rough surfaces have attracted a lot of attention in recent years due to the development of computational electromagnetic (CEM) for a variety of applications such as target recognition [1–3], environment detection [4], microwave remote sensing [5–7], spectra estimation [8,9], and so on. The classical algorithms have been greatly enhanced by combining them with acceleration approaches. In [4], for example, the method of moments (MOM) is used with the sparse matrix canonical grid approach to speed up matrix column multiplications. In [10–12], the finite difference time domain approach (FDTD) is utilized with the perfectly matched layer absorbing boundary to compute the composite EM scattering from varied dimensions of rough surfaces. Ref. [13] employs the domain decomposition methodology in conjunction with the finite element method (FEM) to solve anisotropic EM scattering issues.

With the focus of research shifting to electrically large targets and enormous rough surfaces, high-frequency approximation approaches with reasonable equivalent models are progressively appearing. For example, ref. [14] presented a hybrid method combining

physical optics (PO) with the four-path model (FPM). Refs. [15,16] modified the FPM to broaden the scope of application. However, because of the intrinsic limits of PO, these approaches may not be suitable for targets with cavities or dihedral structures. The shooting and bouncing rays (SBR) method, which combines the benefits of geometrical optics (GO) and PO, was presented in [17] to overcome these challenges. The SBR method is now extensively used and developed in many ways. To estimate the composite EM scattering from an electrically large and complex platform, ref. [18] used the SBR method hybridized with MOM. Ray tracing's temporal effectiveness is increased with OpenGL [19] and the Kd-tree structure [20]. The near-field EM scattering from the frequency domain [21] and time domain [22,23] was extended to the SBR method's application scope. The composite EM scattering from multiple targets above the sea surface was studied using the SBR method and the two scale models (TSM) hybrid model in [24].

However, the processed rough surface in all of the literature mentioned above is either sea or ground surface, which only comprises one background surface type. The dihedral structures are only present in targets. In the actual radar detection situation, it is feasible for both different types of rough surfaces to coexist in a single radar beam. Ref. [25] implements a hybrid iterative solution to simulate composite rough surface EM scattering in a circular water zone encased within a sizable land rough surface. Ref. [26] calculates the EM scattering of an island's composite rough surface in deep water. Refs. [27–29] researched coastal environment composite scattering using various hybrid techniques. A type of environment with a natural semi-enclosed cavity structure exists, although little study has been done on it. The canyon/valley environment serves as a good example. Aircraft and missiles can evade radar detection by flying in a canyon or valley. At the same time, the defense side needs to research the composite scattering characteristics in such scenarios to improve the defense ability. Our study team proposed several methods for the issue. Ref. [30] studied the composite EM scattering characteristics from a target above a valley environment based on the SBR method and ray-density normalization concept. However, the valley, which is with an arched bottom, was not a typical type. In addition, the scattering from the rough surface was calculated coarsely. Traditional SBR method was used to calculate the properties of EM scattering in mountainous regions without taking targets into account in [31].

This article aims to investigate a method for modeling the canyon/valley environment appropriately, obtaining the composite EM scattering from a target above the canyon/valley environment efficiently. Meanwhile, full explorations and discussions of the composite scattering characteristics are necessary. Accordingly, the contributions and work of this article mainly include the following four parts:

1. Based on the composite surface modeling theory, a method for modeling the canyon/valley environment is suggested, which can realize the typical composite rough surface containing two slopes and a bottom.
2. The traditional SBR algorithm is modified by introducing the high-order reflection model, which considers the roughness of the composite rough surface for EM scattering prediction.
3. The facet-based small slope approximation (FBSSA) scattering model combined with the modified SBR algorithm is proposed to calculate the composite EM scattering from a complex target above the canyon/valley environment, which has better computation accuracy without a noticeable increase in memory and time consumption.
4. In the framework of the environment modeling method and modified SBR-FBSSA algorithm, thorough analyses of the composite EM scattering characteristics of a target above the canyon/valley environment were carried out. We also investigated how the Brewster effect affects the canyon's or valley's EM scattering characteristics. A more intricate scattering mechanism will result from the complex target in this canyon/valley environment.

Researching these scattering issues is essential from a practical standpoint; this article's discussions, distinct occurrences, and findings will give the radar detection and remote sensing industries a solid data foundation.

The remainder of this article is organized as follows. In Section 2, the weighted composite rough surface contour function is introduced, and canyon/valley composite rough surface modeling is presented. Section 3 presents the composite scattering model of the ultra-low target above the canyon/valley environment and the modified SBR-FBSSA method. Verifications and numerical simulation results are presented and discussed in Section 4. Section 5 is devoted to the conclusions of this paper.

2. Canyon/Valley Composite Rough Surface Modeling

As shown in Figure 1, the canyon/valley environment has a natural semi-enclosed cavity structure. The sides are often terrestrial settings with varying slope degrees, while the bottom surface may be an aquatic or terrestrial environment. We designate the composite rough surface with a terrestrial bottom as a canyon and a water environment as a valley to make descriptions more convenient.



(**a**) (**b**)

Figure 1. Natural canyon and valley environment: (**a**) canyon with terrestrial bottom; (**b**) valley with water bottom.

When modeling the canyon/valley composite rough surface, the terrestrial parts of the environment can be simulated using Gaussian rough surfaces with the expression of the Gaussian spectral function as [32]

$$W_{\text{Gauss}}(k_x, k_y) = \frac{l_x l_y h_{\text{rms}}^2}{4\pi} \exp\left(-\frac{k_x^2 l_x^2}{4} - \frac{k_y^2 l_y^2}{4}\right) \tag{1}$$

where h_{rms} denotes the root mean square (RMS) height of the rough surface, which is used to quantify the fluctuation range of the rough surface, and l_x and l_y are the correlation lengths of the rough surface in x- and y- dimensions, respectively.

By using Pierson-Moskowitz (PM) sea surface [33], the water component environment may be reproduced, and the expression for the PM spectrum function is

$$W_{\text{PM}}(k) = \frac{\alpha_p}{2k^3} \exp\left(-\frac{\beta g^2}{v_{19.5}^4 k^2}\right) \tag{2}$$

where $k^2 = k_x^2 + k_y^2$, $\alpha_p = 8.10 \times 10^{-3}$, $\beta = 0.74$, g is the acceleration of gravity $g = 9.81$ m/s^2, and the $v_{19.5}$ is the wind velocity 19.5 m above the sea surface. It should be pointed out that when the wind velocity is small, the water surface is calm enough, and the waves on the water surface are slight. So the approximation of the water component environment is reasonable. In this paper, the wind velocities are set 1 m/s, 0.6 m/s and 0.2 m/s.

By adjusting parameter values and combining the aforementioned spectral functions, rough surfaces with various statistical properties can be simulated using the Monte Carlo approach.

The rough surface contour function can be represented by using the fast Fourier transform as follows.

$$f(x,y) = \frac{1}{L_x L_y} \sum_{m=-\infty}^{\infty} \sum_{n=-\infty}^{\infty} b_{mn} \exp\left(\frac{\mathrm{j}2\pi mx}{L_x}\right) \exp\left(\frac{\mathrm{j}2\pi ny}{L_y}\right) \tag{3}$$

$$b_{mn} = 2\pi\sqrt{L_x L_y W(k)} \times \begin{cases} \frac{N(0,1)+\mathrm{j}N(0,1)}{\sqrt{2}} & m \neq 0, N_x/2, n \neq 0, N_y/2 \\ N(0,1) & m = 0, N_x/2 \text{ or } n = 0, N_y/2 \end{cases} \tag{4}$$

where $N(0,1)$ denotes random points following standard normal distribution, L_x and L_y represent the simulated rough surface lengths in x- and y-dimensions, respectively; and N_x and N_y are the number of sampling points in x- and y-dimensions.

The canyon/valley composited rough surface can be regarded as the composite of three parts of the rough regional surface. We present three sets of weighting functions to weigh the connection of various areas of the rough surfaces, ensuring that the rough surfaces of different regions may preserve their distinct statistical properties and the transition regions are smoothly connected while compounding. The following are the fundamental formulae for the weighted composite rough surface contour function:

$$\begin{cases} f_{\mathrm{com}}(x,y) = f_{\mathrm{sur1}}(x,y) \cdot w_1 + f_{\mathrm{sur2}}(x,y) \cdot w_2 + f_{\mathrm{sur3}}(x,y) \cdot w_3 \\ w_1 = \frac{[\pi/2+\arctan(y-y_1)]}{\pi} \\ w_2 = \frac{[\pi/2-\arctan(y-y_1)]}{\pi} \cdot \frac{[\pi/2+\arctan(y-y_2)]}{\pi} \\ w_3 = \frac{[\pi/2-\arctan(y-y_2)]}{\pi} \end{cases} \tag{5}$$

where y_1 and y_2 denote the location of the boundary line of different types of rough surfaces, which may be altered based on actual needs; $f_{\mathrm{sur1}}(x,y)$, $f_{\mathrm{sur2}}(x,y)$, and $f_{\mathrm{sur3}}(x,y)$ are different rough surfaces following different statistical features, respectively. The environment of a canyon or valley typically has a particular slope on both sides, and (5) can be further modified as

$$\begin{cases} f_{\mathrm{c/v}}(x,y) = [f_{\mathrm{sur1}}(x,y) + k_1 y] \cdot w_1 + f_{\mathrm{sur2}}(x,y) \cdot w_2 + [f_{\mathrm{sur3}}(x,y) + k_3 y] \cdot w_3 \\ w_1 = \frac{[\pi/2+\arctan(y-y_1)]}{\pi} \\ w_2 = \frac{[\pi/2-\arctan(y-y_1)]}{\pi} \cdot \frac{[\pi/2+\arctan(y-y_2)]}{\pi} \\ w_3 = \frac{[\pi/2-\arctan(y-y_2)]}{\pi} \\ k_1 = -\tan(\frac{\alpha_1}{180^\circ} \cdot \pi) \\ k_3 = \tan(\frac{\alpha_3}{180^\circ} \cdot \pi) \end{cases} \tag{6}$$

where $f_{\mathrm{c/v}}(x,y)$ denotes the surface profile distribution of the canyon/valley rough surface, and α_1 and α_3 are the slope angles of the canyon/valley sides.

Figure 2 depicts a brief diagram of how weighted functions operate. The $\alpha_1 = 30^\circ$, $\alpha_3 = 45^\circ$, boundary lines $y_1 = -10$ m and $y_2 = 10$ m. At first, the three plates' height is 0 m. The surfaces on each side of the boundary lines are joined smoothly when the weighted function has completed its task. Two slopes outside of the boundaries appear at the same time.

The composite rough surfaces of a simulated canyon and valley are shown in Figure 3. The size of the canyon/valley rough surface is $L_x \times L_y$: 40 m × 60 m, the boundary lines $x_1 = -10$ m and $x_2 = 10$ m, and the correlation length of the rough is $l_x \times l_y$: 2 m × 2 m. Set the RMS height $h_{\mathrm{rms}} = 0.3$ m, the wind velocity 19.5 m above the sea surface $v_{19.5} = 1$ m/s.

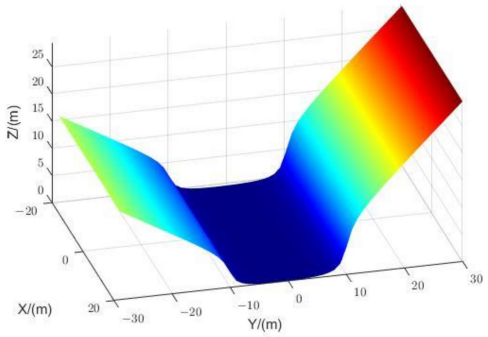


Figure 2. Sketch map of composite plate derived by weighted function.

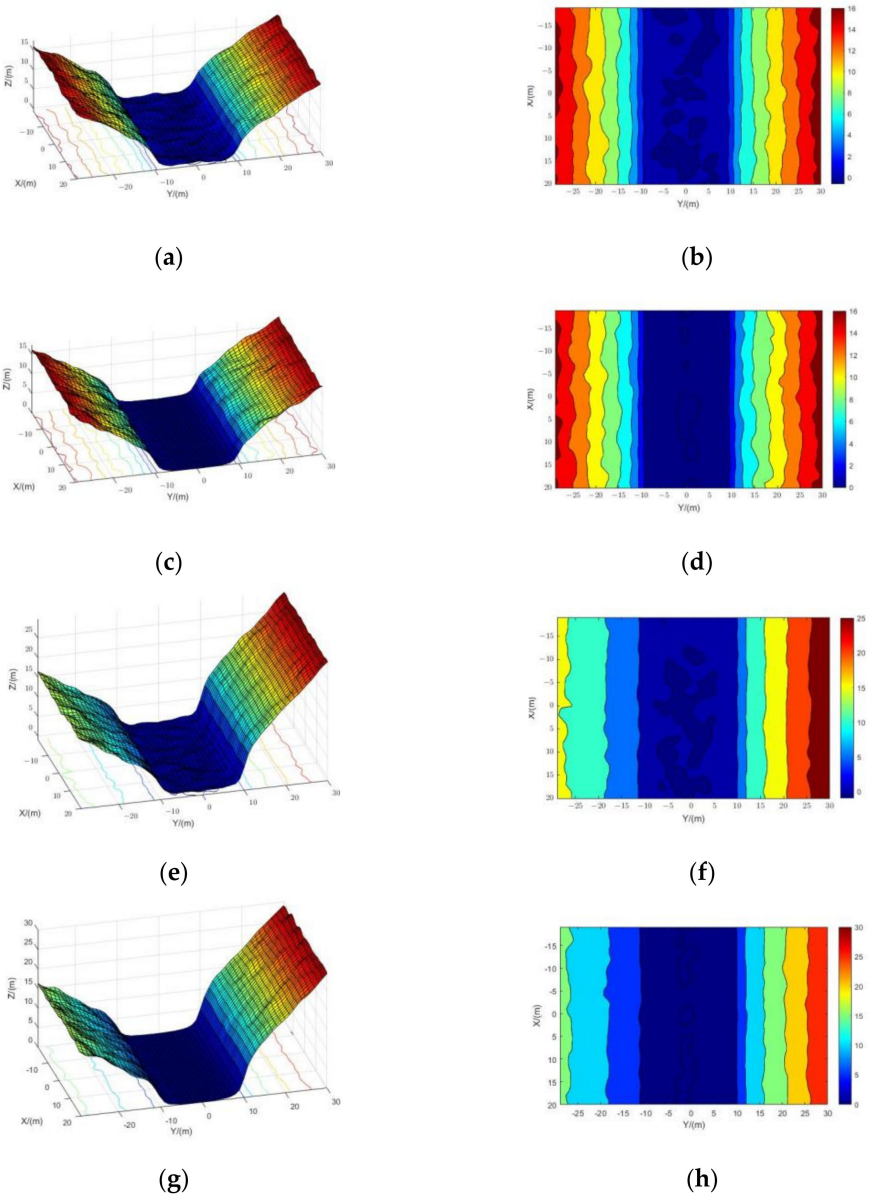


Figure 3. Canyon and valley composite rough surface simulation results: (**a**) geometry of canyon, $\alpha_1 = 30°$, $\alpha_3 = 30°$; (**b**) contour map of canyon, $\alpha_1 = 30°$, $\alpha_3 = 30°$; (**c**) geometry of valley, $\alpha_1 = 30°$, $\alpha_3 = 30°$; (**d**) contour map of valley, $\alpha_1 = 30°$, $\alpha_3 = 30°$; (**e**) geometry of canyon, $\alpha_1 = 30°$, $\alpha_3 = 45°$; (**f**) contour map of canyon, $\alpha_1 = 30°$, $\alpha_3 = 45°$; (**g**) geometry of valley, $\alpha_1 = 30°$, $\alpha_3 = 45°$; (**h**) contour map of valley, $\alpha_1 = 30°$, $\alpha_3 = 45°$.

Figure 3 illustrates how effectively the simulation results may capture the geometrical features of a canyon/valley composite rough surface. Different canyon/valley environments may be represented by altering the parameters.

3. Modified SBR-FBSSA Method for Composite Scattering

3.1. Composite Scattering Model of Target above Canyon/Valley Environment

The composite scattering model for an ultra-low target above the canyon/valley is depicted in Figure 4 as operating inside the modified SBR-FBSSA technique framework. It is composed of five main components.

1. Direct scattering from the ultra-low target, denoted by C1.

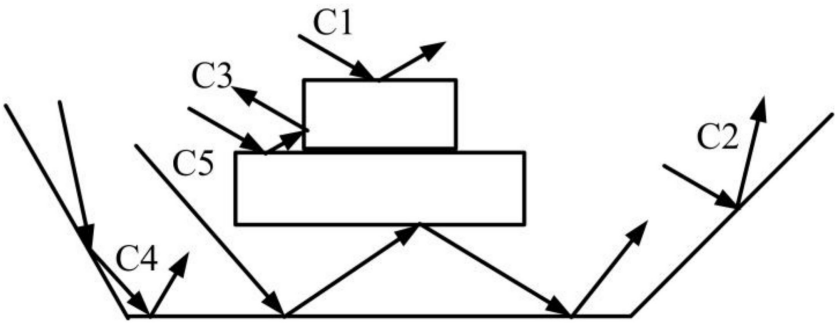


Figure 4. Illustration of SBR-FBSSA composite scattering model for canyon/valley environment.

This part is calculated by the SBR method. Not only should the target's self-occlusion be taken into account throughout the computation, but also the target's and the composite surface's mutual occlusion. Moreover, the scattering caused by the edge structure should not be neglected. This paper adopts the method of equivalent currents to improve the scattering results.

2. Direct scattering from composite rough surface, denoted by C2.

The facet-based small-slope approximation (FBSSA) method is adapted to calculate the direct scattering from the canyon/valley rough surface. The composite surface, which is created in Section 2, has numerous facets. The small slope approximation method in the local coordinate system determines the scattering field for each facet. The vector superposition of the facet-scattering fields in a global coordinate system defines the total scattering field. In a similar vein, mutual and self-occlusion should be considered.

3. Multiple scattering from the target, denoted by C3.

This part is calculated by the SBR method. Ultra-low targets usually contain complex structures, similar to dihedrals, which can cause multiple reflections. This interactional component will produce strong scattering fields. Thus, it is necessary to calculate multiple scattering from the target.

4. Multiple scattering from canyon/valley composite rough surface, denoted by C4.

In contrast to typically terrestrial environments, sea surfaces, and other composite rough surfaces, canyon/valley environments have a natural cavity structure that is semi-enclosed. Due to the multiple scattering from the environment, the particular structure increases the complexity of the composite scattering. To calculate this portion of composite scattering, a modified SBR method is implemented.

5. Coupling scattering between the target and canyon/valley composite rough surface, denoted by C5.

In the composite scattering model, coupling scattering between the target and environment is commonly present. Higher-order reflection makes the coupling between the target and canyon/valley more complex, which could be solved well and efficiently by utilizing the modified SBR algorithm.

It is worth noting that the MSBR method is improved by replacing the Snell reflection coefficients in the traditional SBR method with a high-order reflection model introduced in Section 3.2. The MSBR method can also handle the cases that the SBR method can handle. At last, components C1, C3, C4, and C5 are calculated by the MSBR method, and component C2 is calculated by FBSSA. As described above, composite scattering can be generated by superimposing the scattering fields that have been acquired.

3.2. Modified SBR Algorithm

The SBR algorithm describes the scattering fields by GO and PO methods. The GO method is utilized to trace the EM wave propagation paths. When the EM waves leave the composite model or finish bouncing, the PO method is used to compute the scattering field.

The incident electric field $\boldsymbol{E}_i^0$ by the plane wave is expressed by

$$\boldsymbol{E}_i^0 = A_i^0 \hat{\boldsymbol{e}}_i^0 e^{j\phi_0} \tag{7}$$

where ϕ_0 denotes the initial phase of $\boldsymbol{E}_i^0$, A_i^0 is the incident wave electric field intensity, and $\hat{\boldsymbol{e}}_i^0$ is the unit vector of vertical-polarization or horizontal-polarization, described by

$$\hat{\boldsymbol{e}}_i^0 = \begin{cases} (\cos\theta_i \cos\varphi_i, \cos\theta_i \sin\varphi_i, -\sin\theta_i) & \text{V-polarization} \\ (-\sin\varphi_i, \cos\varphi_i, 0) & \text{H-polarization} \end{cases} \tag{8}$$

where the incident pitch angle and azimuth angle are denoted by θ_i and φ_i, respectively.

As shown in Figure 5, assuming the i-th reflection point P_i located at the facet S_n with the normal direction $\hat{n}_i$, θ_i and θ_r are the incident- and reflect-pitch angles, respectively, $\hat{\boldsymbol{R}}_i$ and $\hat{\boldsymbol{R}}_r$ are the incident- and reflect-unit vector, respectively, and P_{i+1} denotes the $(i+1)$-th reflection point. Based on the GO method,

$$\begin{cases} \theta_r = \theta_i \\ \hat{\boldsymbol{R}}_r = \hat{\boldsymbol{R}}_i - 2(\hat{\boldsymbol{R}}_i \cdot \hat{\boldsymbol{n}}_i) \\ \boldsymbol{E}_i'(\boldsymbol{r}_{p_i}) = E_v \hat{\boldsymbol{e}}_v + E_h \hat{\boldsymbol{e}}_h \\ \boldsymbol{E}_r'(\boldsymbol{r}_{p_i}) = (DF)_i (R_v E_v \hat{\boldsymbol{e}}_v + R_h E_h \hat{\boldsymbol{e}}_h) \end{cases} \tag{9}$$

where $\boldsymbol{E}_i'(\boldsymbol{r}_{p_i})$ and $\boldsymbol{E}_r'(\boldsymbol{r}_{p_i})$ denote the incident- and reflect-electric field, respectively. The subscripts v and h denote the vertical- and horizontal-polarization mode, $(DF)_i$ represents the diffusion coefficient [34] at the point P_i.

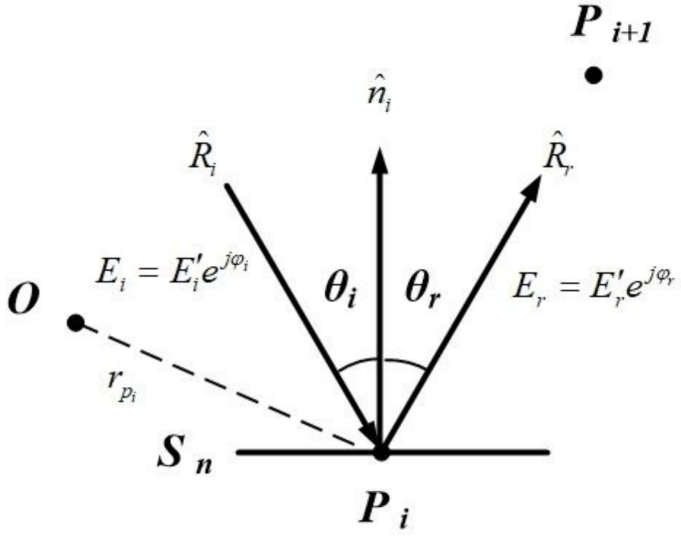


Figure 5. Sketch map of the i-th reflection on the facet S_n.

In traditional SBR method, the R_v and R_h are Snell reflection coefficients meaning the facets of the rough surface are considered smooth planes. However, the facets of rough surfaces are rough in practice. Hence, this situation is considered in our modified SBR method by introducing a high-order reflection model R_p as follows [35]

$$R_p = \rho_S \left(R_{p00} + m^2 \left(R_{p02} + R_{p20} \right) \right) \tag{10}$$

where subscript p denotes the polarization mode, is v- or h-; m is the root mean square slope [36], and ρ_S is described as

$$\rho_S = \begin{cases} \exp\left[(-2\pi\tau)^2 \right] & 0 \le \tau \le 0.1 \\ 0.812537 / \left[1, +, 2, (2\pi\tau)^2 \right] & \tau \ge 0.1 \end{cases} \tag{11}$$

where $\tau = h_{rms} \cos\theta_i / \lambda$, λ is the wavelength. Continually, R_{p00}, R_{p02} and R_{p20} are Taylor coefficients of the local reflection coefficient. For v-polarization, these Taylor coefficients can be obtained by:

$$\begin{cases} R_{v00} = \frac{\eta_1 \cos\theta_i - \eta_2 \cos\theta_t}{\eta_1 \cos\theta_i + \eta_2 \cos\theta_t} \\ R_{v10} = \frac{\left(\eta_1 \sin\theta_i (1 - R_{v00}) - \eta_2 \frac{k_1 \cos\theta_i}{k_2 \cos\theta_t} \sin\theta_t (1 + R_{v00}) \right)}{(\eta_1 \cos\theta_i + \eta_2 \cos\theta_t)} \\ R_{v02} = \frac{-\eta_2 \left(1 - k_1^2 / k_2^2 \right) (1 + R_{v00})}{2(\eta_1 \cos\theta_i + \eta_2 \cos\theta_t) \cos\theta_t} \\ R_{v20} = \frac{R_{v02}}{\cos^2\theta_t} - R_{v10} \frac{\eta_1 \sin\theta_i + \eta_2 \frac{k_1 \cos\theta_i}{k_2 \cos\theta_t} \sin\theta_t}{\eta_1 \cos\theta_i + \eta_2 \cos\theta_t} \end{cases} \tag{12}$$

where η_1 and η_2 are the impedances of the air and rough surface medium, respectively; k_1 and k_2 are wave numbers corresponding; θ_i and θ_t are incident and transmission angles, simultaneously, θ_i and θ_t obey Snell's Law.

Similarly, for h-polarization, the expressions are

$$\begin{cases} R_{h00} = \frac{\eta_2 \cos\theta_i - \eta_1 \cos\theta_t}{\eta_2 \cos\theta_i + \eta_1 \cos\theta_t} \\ R_{h10} = \frac{\left(\eta_2 \sin\theta_i (1 - R_{h00}) - \eta_1 \frac{k_1 \cos\theta_i}{k_2 \cos\theta_t} \sin\theta_t (1 + R_{h00}) \right)}{(\eta_2 \cos\theta_i + \eta_1 \cos\theta_t)} \\ R_{h02} = \frac{-\eta_1 \left(1 - k_1^2 / k_2^2 \right) (1 + R_{h00})}{2(\eta_2 \cos\theta_i + \eta_1 \cos\theta_t) \cos\theta_t} \\ R_{h20} = \frac{R_{h02}}{\cos^2\theta_t} - R_{h10} \frac{\eta_2 \sin\theta_i + \eta_1 \frac{k_1 \cos\theta_i}{k_2 \cos\theta_t} \sin\theta_t}{\eta_2 \cos\theta_i + \eta_1 \cos\theta_t} \end{cases} \tag{13}$$

According to the GO method, the i-th incident electric field at each reflection point can be used to compute the i-th reflected electric field. Meanwhile, the $(i + 1)$-th incident electric field is obtained using the i-th reflected electric field. The field and path tracing can be realized utilizing such sequential calculation.

After the ray tracing, the scattering field is calculated by the PO method

$$\boldsymbol{E}^{\mathrm{s}} \approx \frac{ik}{4\pi} \cdot \frac{e^{-ikr}}{r} [\hat{\boldsymbol{s}} \times (\boldsymbol{M}_{\mathrm{s}} + \eta_0 \hat{\boldsymbol{s}} \times \boldsymbol{J}_{\mathrm{s}})] \cdot \Delta\mathrm{A} \cdot I \tag{14}$$

where $\boldsymbol{J}_{\mathrm{s}}$ and $\boldsymbol{M}_{\mathrm{s}}$ denote electric current and magnetic current on the facet, k is the wave number, $\hat{\boldsymbol{s}}$ represents the unit vector of observation direction, and r indicates the distance from the original point to a point located in the facet. ΔA denotes the area of the facet; I can be calculated by the Gordon method in [37].

Since the realistic targets may have many edge structures, the diffraction cannot be neglected. In this paper, the method of equivalent current is utilized to calculate the contribution of the edge.

$$\boldsymbol{E}^{\mathrm{d}} = \frac{\mathrm{j}k}{4\pi}\frac{e^{-\mathrm{j}kr}}{r}\int_{C}\left\{\eta_0\hat{\mathbf{s}}\times[\hat{\mathbf{s}}\times\boldsymbol{J}(\boldsymbol{r}')]+\hat{\mathbf{s}}\times\boldsymbol{M}(\boldsymbol{r}')\right\}e^{\mathrm{j}k\hat{\mathbf{s}}\cdot\boldsymbol{r}'}dl \tag{15}$$

where η_0 denotes the wave impedance. $\boldsymbol{J}(\boldsymbol{r}')$ and $\boldsymbol{M}(\boldsymbol{r}')$ denote the equivalent electric and magnetic current, respectively, and $\boldsymbol{r}'$ denotes vector from the original point to a point located in edge C. $\boldsymbol{J}(\boldsymbol{r}')$ and $\boldsymbol{M}(\boldsymbol{r}')$ can be found in [38].

Based on (7)–(15), the scattering field $\boldsymbol{E}^{\mathrm{MSBR}}$ including direct scattering from the target (as well as the diffraction field), multiple scattering from the target, multiple scattering from canyon/valley composite rough surface, and coupling scattering between the target and canyon/valley composite rough surface can be written as

$$\boldsymbol{E}^{\mathrm{MSBR}} = \boldsymbol{E}^{\mathrm{s}} + \boldsymbol{E}^{\mathrm{d}} \tag{16}$$

3.3. Facet-Based Small Slope Approximation Scattering Model

First, we introduce the geometrical configuration of the scattering problem of canyon/valley composite rough surfaces. As shown in Figure 6, the global coordinate system is defined as $(\boldsymbol{x},\boldsymbol{y},\boldsymbol{z})$, $\boldsymbol{k_i}$ and $\boldsymbol{k_s}$ denote incident and scattering wave vector respectively, $\boldsymbol{q} = \boldsymbol{k_s} - \boldsymbol{k_i}$, θ_i and θ_s are the pitch incident and scattering angles, and φ_i and φ_s are the azimuth incident and scattering angles. The composite surface elevation is described by $h(\boldsymbol{r}) = h(x,y)$, where $\boldsymbol{r}$ is the $x-y$ plane component of the position vector $R = (\boldsymbol{r},z)$. Similarly, the local coordinate system is defined as $(\hat{\boldsymbol{x}}_l,\hat{\boldsymbol{y}}_l,\hat{\boldsymbol{z}}_l)$, which is located at the facet related by $h_l(\boldsymbol{r}_l) = h_l(x_l,y_l)$, and vector $\boldsymbol{r}_l$ denotes the $x_l - y_l$ plane component of the position, $\hat{\boldsymbol{n}}$ is the normal unit vector of the local facet, and $\boldsymbol{R}_l$ is the position vector of its center. Within the local coordinate system, $\boldsymbol{k}_{il} = (\boldsymbol{p}_{il},-q_{il})$ and $\boldsymbol{k}_{sl} = (\boldsymbol{p}_{sl},q_{sl})$ are the incident and scattering wave vectors, the vector $\boldsymbol{p}_{il}$ and $\boldsymbol{p}_{sl}$ are the $x_l - y_l$ components, and q_{il} and q_{sl} are the values of corresponding z_l components.

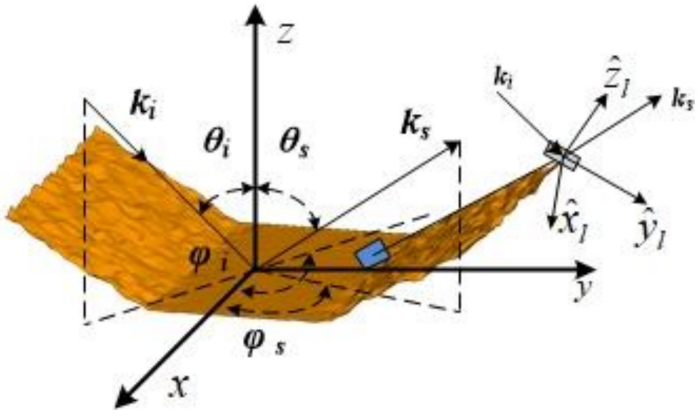


Figure 6. The geometrical configuration of the scattering problem.

As for the local coordinate system, we can define that

$$\begin{cases} \boldsymbol{z}_l = \hat{\boldsymbol{n}}, \\ \boldsymbol{y}_l = \frac{\boldsymbol{k}_i\times\hat{\boldsymbol{n}}}{|\boldsymbol{k}_i\times\hat{\boldsymbol{n}}|}, \\ \boldsymbol{x}_l = \boldsymbol{y}_l\times\boldsymbol{z}_l \end{cases} \tag{17}$$

The traditional facet-based scattering model combines the two-scale method based on the Kirchhoff Approximation (KA) and the Small Perturbation Method (SPM) to describe the scattering problems of the composite surface. While these two methods have certain

applicable conditions, Voronovich [39] pointed out that the appropriate requirements of these two methods could not cover all rough scale cases. Small slope approximation (SSA) is suitable for the electromagnetic scattering problem from rough surfaces satisfying the KA and SPM and for the transition type of rough surfaces. What's more, in the facet-based model which contains the SSA, the facets are treated as rough surfaces instead of smooth plates [39].

For the SSA, the scattering amplitude of the facet S_n in the local coordinate system is given as

$$\boldsymbol{S}_l(\boldsymbol{k}_{sl}, \boldsymbol{k}_{il}) = \frac{2(q_{sl}q_{il})^{1/2}}{q_{sl}+q_{il}}\boldsymbol{B}(\boldsymbol{k}_{sl}, \boldsymbol{k}_{il}) \times \int \frac{d\boldsymbol{r}_l}{(2\pi)^2} \exp[-\mathrm{i}(p_{sl}-p_{il})\cdot \boldsymbol{r}_l + j(q_{sl}+q_{il})h(\boldsymbol{r}_l)]d\boldsymbol{r}_l \quad (18)$$

where $\boldsymbol{B}$ is local polarization factors, the relation between $\boldsymbol{B}$ and global polarization factors $\boldsymbol{F}$ is as follows [40]

$$\begin{bmatrix} F_{VV} & F_{VH} \\ F_{HV} & F_{HH} \end{bmatrix} = \begin{bmatrix} \hat{\boldsymbol{v}}_s \cdot \hat{\boldsymbol{v}}_s^{'} & \hat{\boldsymbol{h}}_s \cdot \hat{\boldsymbol{h}}_s^{'} \\ \hat{\boldsymbol{v}}_s \cdot \hat{\boldsymbol{h}}_s^{'} & \hat{\boldsymbol{h}}_s \cdot \hat{\boldsymbol{v}}_s^{'} \end{bmatrix} \begin{bmatrix} B_{vv} & B_{vh} \\ B_{\mathrm{m}} & B_{hh} \end{bmatrix} \begin{bmatrix} \hat{\boldsymbol{v}}_i \cdot \hat{\boldsymbol{v}}_i^{'} & \hat{\boldsymbol{h}}_i \cdot \hat{\boldsymbol{h}}_i^{'} \\ \hat{\boldsymbol{v}}_i \cdot \hat{\boldsymbol{h}}_i^{'} & \hat{\boldsymbol{h}}_i \cdot \hat{\boldsymbol{v}}_i^{'} \end{bmatrix} \quad (19)$$

where $\left[\hat{\boldsymbol{h}}_{\boldsymbol{i}}^{'}, \hat{\boldsymbol{v}}_{\boldsymbol{i}}^{'}, \hat{\boldsymbol{h}}_{\boldsymbol{s}}^{'}, \hat{\boldsymbol{v}}_{\boldsymbol{s}}^{'}\right]$ and $\left[\hat{\boldsymbol{h}}_{\boldsymbol{i}}, \hat{\boldsymbol{v}}_{\boldsymbol{i}}, \hat{\boldsymbol{h}}_{\boldsymbol{s}}, \hat{\boldsymbol{v}}_{\boldsymbol{s}}\right]$ are unit polarization vectors in local- and global-coordinate systems.

According to the [41], the normalized radar cross section (NRCS) can be expressed as

$$\sigma_n = q_{sl}q_{il}\left\langle \boldsymbol{S}_l(\boldsymbol{k}_{sl}, \boldsymbol{k}_{il}) - \langle \boldsymbol{S}_l(\boldsymbol{k}_{sl}, \boldsymbol{k}_{il})\rangle \times (\boldsymbol{S}_l(\boldsymbol{k}_{sl}, \boldsymbol{k}_{il}) - \langle \boldsymbol{S}_l(\boldsymbol{k}_{sl}, \boldsymbol{k}_{il})\rangle)^* \right\rangle \quad (20)$$

where $\langle\cdot\rangle$ denotes the ensemble average, * denotes the conjugate.

This model only provides the scattering amplitude information of the local facet element of the rough surface but does not contain the phase information. The scattering field can be expressed as

$$\boldsymbol{E}_n = \frac{\exp(\mathrm{j}kR_l)}{R_l}\sqrt{\frac{\Delta \mathrm{A}}{4\pi}\sigma_n} \quad (21)$$

where ΔA is the facet area. The total direct scattering field from the composite rough surface is

$$\boldsymbol{E}^{FBSSA} = \sum_{n=1}^{N} \boldsymbol{E}_n \quad (22)$$

According to (16) and (22), the composite scattering field can be expressed as

$$\boldsymbol{E}^{Total} = \boldsymbol{E}^{MSBR} + \boldsymbol{E}^{FBSSA} \quad (23)$$

4. Simulation and Discussion

In this section, the effectiveness and accuracy of the modified SBR-FBSSA algorithm proposed in this article are verified by comparison with the multilevel fast multiple algorithm (MLFMA) and the SBR-TSM method proposed in [24] recently. Then, we investigate the impact of various bottom surfaces, slope angles, surface roughness variations, incident azimuth- and pitch-angle variations, as well as the target, on the composite scattering characteristics of the canyon/valley composite rough surfaces.

All simulation results are statistically averaged across 30 samples in this section. Windows 7 with an Intel(R) Xeon(R) Silver 4110 CPU running at 2.10 GHz and 128 GB of RAM serves as the computing platform.

Before proceeding with the algorithm verification in Section 4.1, we illustrate the identical simulation setups in Sections 4.2–4.8. The size of the composite rough surface is set to $L_x \times L_y = 20\ \mathrm{m} \times 60\ \mathrm{m}$, $l_x \times l_y = 2\ \mathrm{m} \times 2\ \mathrm{m}$, the boundary lines located at $y = \pm 10$ m. The working frequency is set as 10 GHz; therefore, the wavelength $\lambda = 0.03$ m and the relative permittivity of the terrestrial surface is (3.0, 0.000036) [42], and the water surface's

is (55.96, 34.95) [24]. The missile-like target is 10 m above the bottom of the canyon/valley composite rough surface, with the size of 5.26 m × 2.82 m × 1.16 m, as shown in Figure 7.

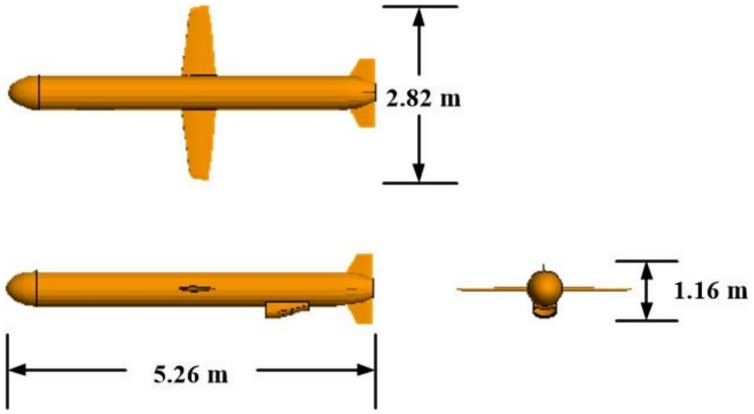


Figure 7. Illustration of dimensions of the missile-like target.

4.1. Verification of Modified SBR-FBSSA Method

In this subsection, the size of the cosine-canyon composite rough surface is set to $L_x \times L_y = 6$ m $\times$ 9 m, $l_x \times l_y = 0.1$ m $\times$ 0.1 m, the boundary lines located at $y = \pm 3$ m, and the slope angles $\alpha_1 = \alpha_3 = 30^\circ$. The work frequency is set as 1 GHz, and the relative permittivity of the terrestrial surface is (8.79, 5.84) [43,44]. The target, a 0.3 m $\times$ 0.6 m $\times$ 0.3 m flare, is 1.5 m above the cosine-canyon composite rough surface. The incident angle is $(\theta_i, \varphi_i) = (-30^\circ, 90^\circ)$ and the observation angles are $(\theta_s, \varphi_s) = (-90^\circ \sim 90^\circ, 90^\circ)$. The illustration of simulation geometry is shown in Figure 8. The bistatic radar cross section (RCS) results in HH- and VV-polarization are shown in Figure 9. Efficiency and accuracy results are listed in Table 1. The maximum error maxγ and average error $\langle\gamma\rangle$ with the total scattering angles N_{θ_s} are taken into the forms as [30]

$$\max\gamma = \max_{\{\theta_s\}} \left| \gamma^T(\theta_s) - \gamma^R(\theta_s) \right| \tag{24}$$

$$\langle\gamma\rangle = \frac{1}{N_{\theta_s}} \sum_{\{\theta_s\}} \left| \gamma^T(\theta_s) - \gamma^R(\theta_s) \right| \tag{25}$$

where γ^R denotes the computation results by MLFMA, which is often used as a standard algorithm, while γ^T denotes the SBR-TSM method or MSBR-FBSSA.

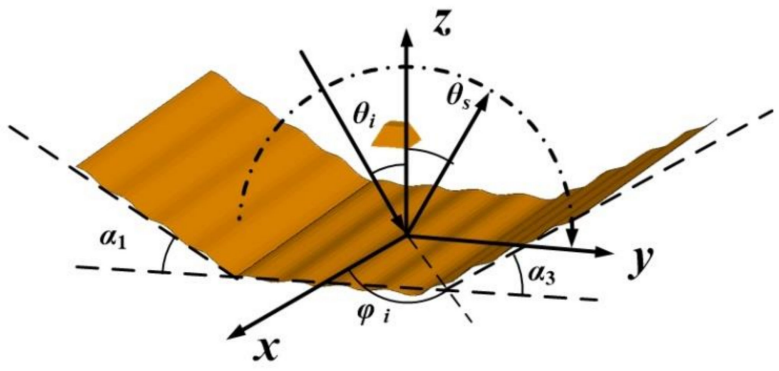


Figure 8. The geometry of a flare above the cosine-canyon composite rough surface.

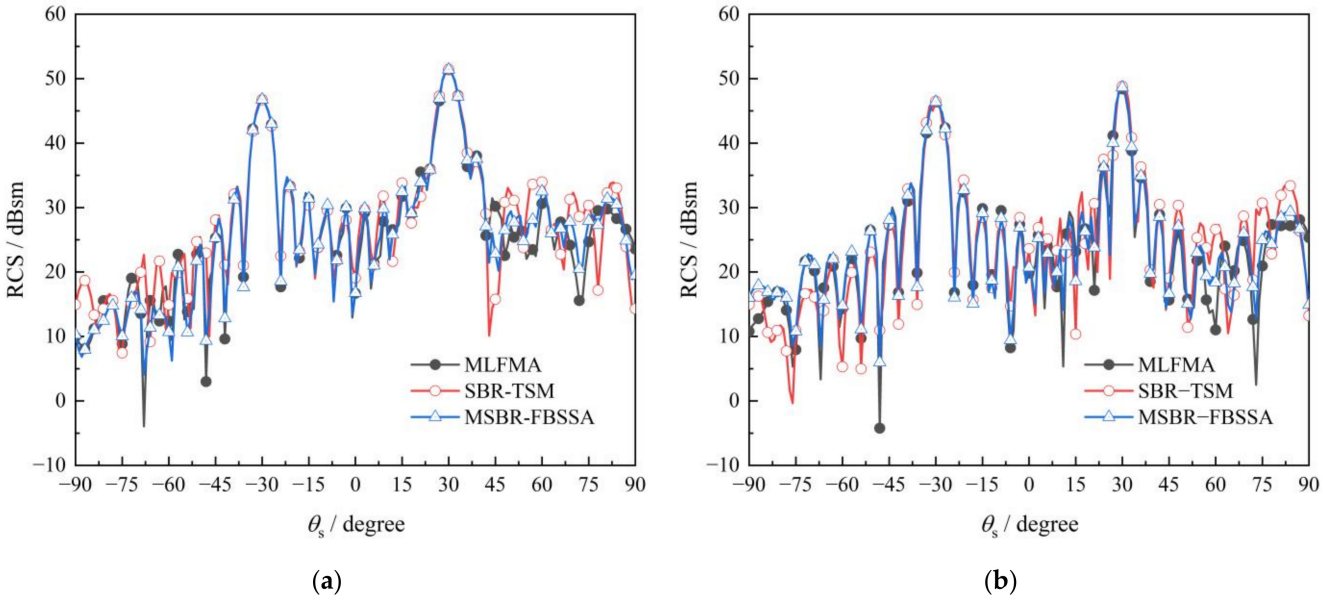


Figure 9. Bistatic RCS of a flare above cosine-canyon composite rough surface: (**a**) HH polarization; (**b**) VV polarization.

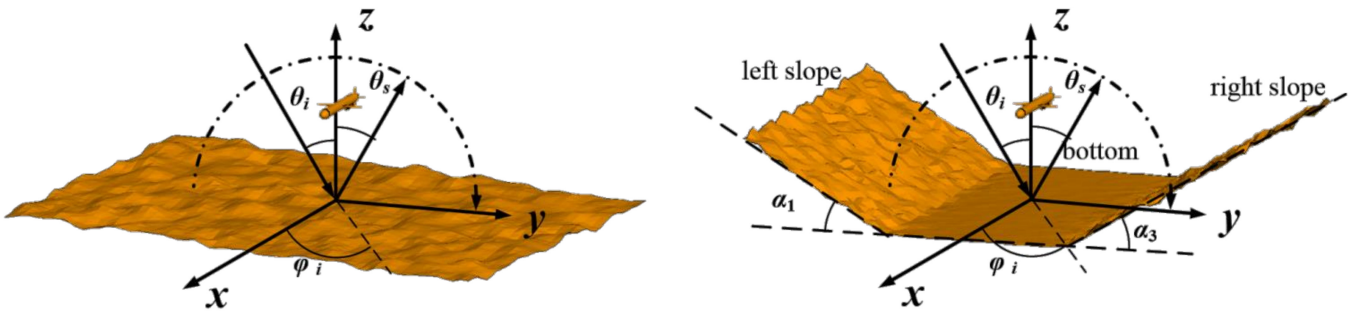
Table 1. Efficiency and accuracy of different algorithms.

Methods	Polarization	Memory (GB)	Time (s)	Maximum Error (dB)	Average Error (dB)
MLFMA	HH	15.236	1251	-	-
	VV	15.373	1264	-	-
SBR-TSM	HH	2.663	87.6	26.60	3.75
	VV	2.679	88.1	27.21	4.18
MSBR-FBSSA	HH	2.703	89.7	9.13	1.63
	VV	2.730	91.3	10.41	1.85

Based on Figure 9 and Table 1, the results calculated by SBR-TSM and MSBR-FBSSA methods are well consistent with the MLFMA's results in $\theta_s = -45^\circ \sim 45^\circ$, while in $\theta_s = -90^\circ \sim -45^\circ$ and $45^\circ \sim 90^\circ$, the MSBR-FBSSA's results displayed the same variation tendency with the standard accurate numerical method MLFMA, while the results by the SBR-TSM method deviate in some angles. From the perspective of the maximum errors, the accuracy of MSBR-FBSSA is improved significantly. Considering the whole angular range and the complexity of the model, the average error can depict the accuracy of the methods in a more practical meaning. Obviously, from the perspective of the average error, our method possesses a better computational accuracy. What's more, considering the memory and time consumption, the algorithm presented in this article does not result in a significant increase in the computational burden. Above all, the efficiency and accuracy of the modified shooting and bouncing rays algorithm combined with the facet-based small slope approximation method developed in this article are verified.

4.2. Composite Scattering of Plain and Valley Composite Rough Surface

This subsection investigates the bistatic composite scattering characteristics of plain and valley composite rough surfaces. The wind speed $v_{19.5} = 0.2$ m/s, and the RMS height $h_{\mathrm{rms}} = 0.2\lambda$. For plain environment, the $\alpha_1 = \alpha_3 = 0^\circ$; for valley environment, the $\alpha_1 = \alpha_3 = 30^\circ$. The illustration of simulation geometry is shown in Figure 10.



(**a**) (**b**)

Figure 10. Illustration of a missile-like target above plain and valley composite rough surface: (**a**) target above plain; (**b**) target above valley.

In Figure 11, the incident angle is $(\theta_i, \varphi_i) = (-30°, 90°)$, the observation angles are $(\theta_s, \varphi_s) = (-90° \sim 90°, 90°)$. The plain and valley RCS curves have a similar trend in most of the angular range. They all peak at $\theta_s = 30°$, which is the specular reflection direction of the plain and the valley's bottom. On both sides of $\theta_s = 30°$, the RCSs decrease gradually with the observation angles varying. Differently, for the scattering of the valley, the curves have other peaks at $\theta_s = 30°$, which are caused by the structure of the right slope. When the incident angle $\theta_i = -30°$, the electromagnetic waves hit the right slope vertically, and the waves are reflected vertically to the source point, causing the peak at $\theta_s = -30°$. Moreover, due to the multiple reflections of incident EM waves inside the semi-enclosed cavity structure of the valley composite rough surface, the RCSs at near $\theta_s = 90°$ are higher than those of plain, which means the scattering power is redistributed because of the unique structure. In a real detection scenario, the number of peaks can help to recognize the plain and valley.

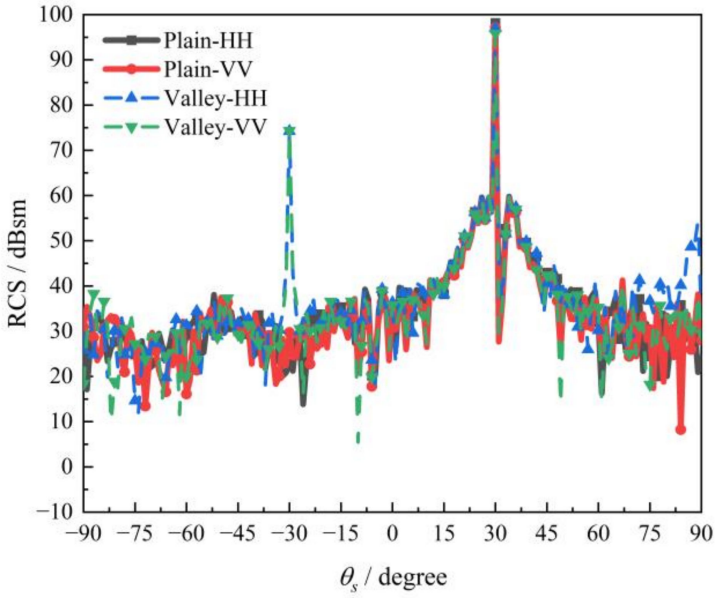


Figure 11. Bistatic RCS results for a missile-like target above plain and valley composite rough surface.

4.3. Composite Scattering of Canyon and Valley Composite Rough Surface

In this example, the bistatic RCS of the canyon and valley environment are investigated. The wind speed $v_{19.5} = 0.2$ m/s, the RMS height $h_{\text{rms}} = 0.2\lambda$, and the slope angles $\alpha_1 = 30°$, $\alpha_3 = 30°$. The illustration of simulation geometry is shown in Figure 12.

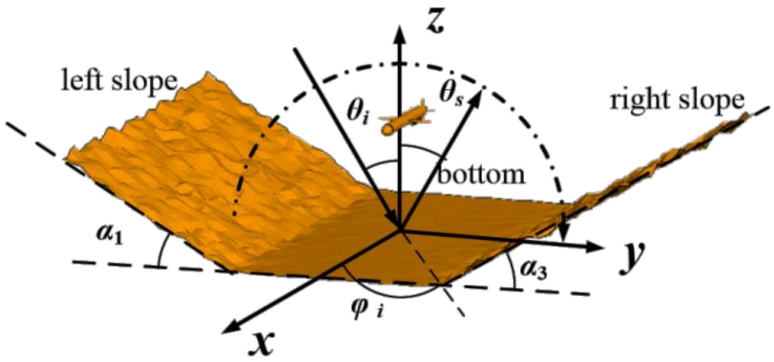


Figure 12. The geometry of the missile-like target above composite rough surface.

In Figure 13, the incident angle is $(\theta_i, \varphi_i) = (-30^\circ, 90^\circ)$, and the observation angles are $(\theta_s, \varphi_s) = (-90^\circ \sim 90^\circ, 90^\circ)$. These RCS curves have the same varying discipline. They both have two peaks; one is the forward scattering's depiction, $\theta_s = 30^\circ$; and the other is the vertical reflection of the right slope $\theta_s = -30^\circ$. However, there is still a noticeable difference in these figures: on two sides of $\theta_s = 30^\circ$, the valley's RCS is much higher than the canyon's. The bottom of the composite rough surfaces' difference could explain the phenomenon. The specular reflection from the bottom contributes the most of the forward scattering at $\theta_s = 30^\circ$. Generally, the specular reflection of a calm water environment is much higher than that of undulating land, which causes the specular reflection from the valley with a water bottom to be stronger than the terrestrial bottom. As for peaks at $\theta_i = -30^\circ$, the same right slope environment makes a similar vertical reflection amplitude. Hence, canyon and valley have similar scattering characteristics, and the differences in the bottom produce the different details between these two types of composite environment. When the environment is detected, the canyon and valley can be distinguished in the forward scattering direction.

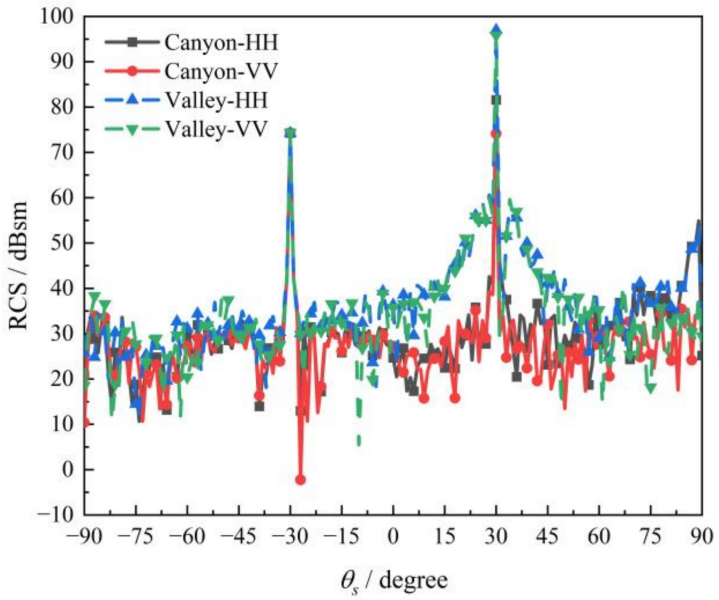


Figure 13. Bistatic RCS for a missile-like target above the canyon and valley composite rough surface.

4.4. Composite Scattering of Canyon/Valley Environment with Different Slope Angles

In this numerical example, the bistatic RCS of the canyon and valley environment are investigated. The RMS height is $h_{\text{rms}} = 0.2\lambda$, the wind speed is $v_{19.5} = 0.2$ m/s. The slope angles are denoted in the figures and table. The incident angle is $(\theta_i, \varphi_i) = (-30^\circ, 90^\circ)$, the observation angles are $(\theta_s, \varphi_s) = (-90^\circ \sim 90^\circ, 90^\circ)$. Figure 14 illustrates the main paths

of the EM wave propagation in canyon/valley composite rough surfaces with different slope-angle combinations. Numerical results are depicted in Figure 15, and the specific peak angles and peak values are listed in Table 2. The illustration of simulation geometry is the same as Section 4.3, shown in Figure 12.

As shown in Figure 15, different slope-angle combinations have different peak angle positions because the EM waves have different propagation paths. First, these five combinations all have peaks at $\theta_s = 30°$, which are caused by the reflection from the bottom. Secondly, when the incident waves strike the slopes with different slope angles, the main paths are different, which makes the RCS prediction difficult. Thirdly, the Brewster effect [16] will affect the peak values, sometimes even making the peak disappear. Comparing Figure 15a's and Figure 15b's $45° - 45°$ curves, both show three peaks at $\theta_s = -60°, 30°, 60°$, respectively. However, the peak value at $\theta_s = 60°$ in VV polarization is much smaller than in HH polarization.

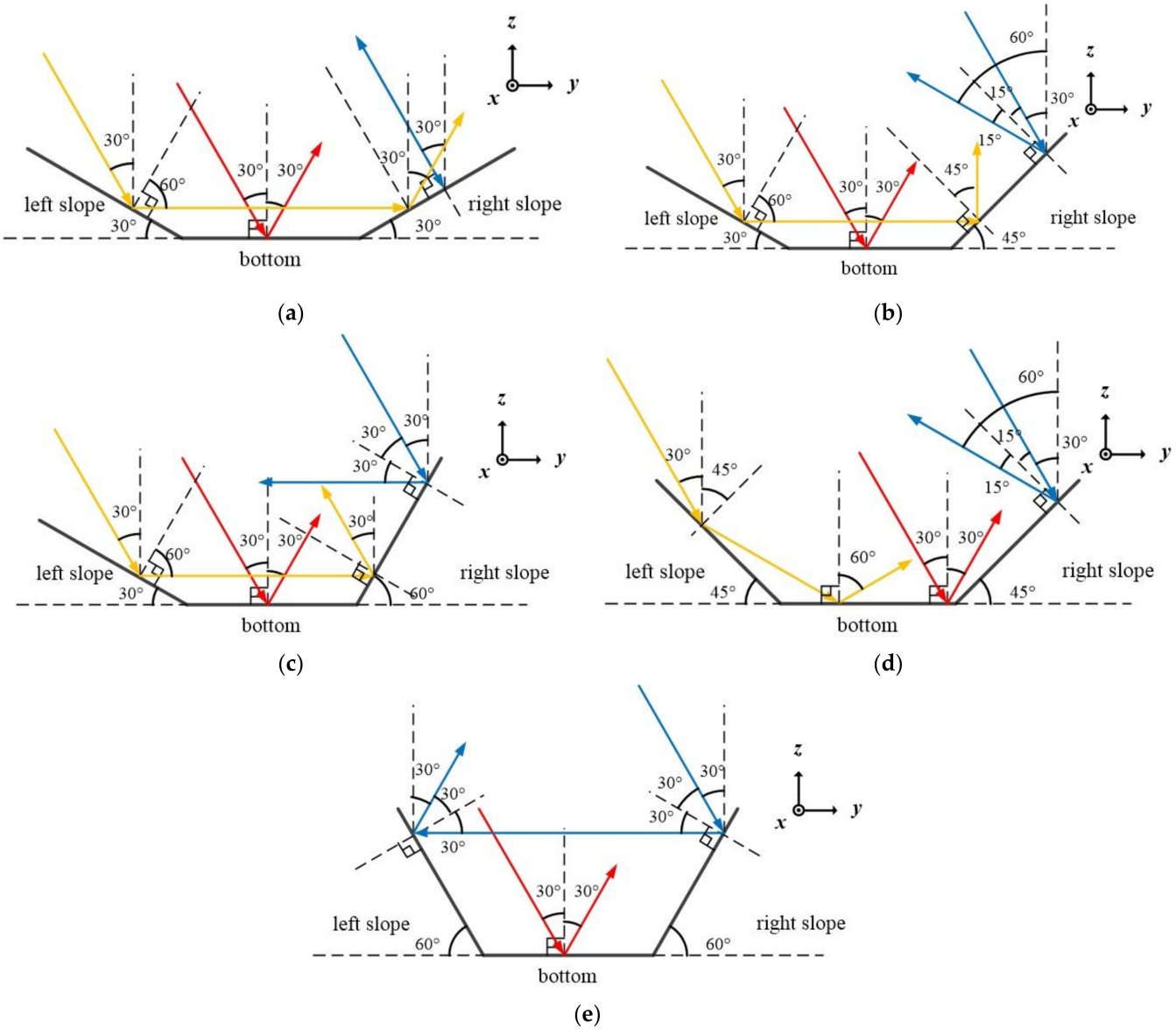


Figure 14. Illustration of EM wave propagation paths in canyon/valley: (**a**) $\alpha_1 = 30°$, $\alpha_3 = 30°$; (**b**) $\alpha_1 = 30°$, $\alpha_3 = 45°$; (**c**) $\alpha_1 = 30°$, $\alpha_3 = 60°$; (**d**) $\alpha_1 = 45°$, $\alpha_3 = 45°$; (**e**) $\alpha_1 = 60°$, $\alpha_3 = 60°$.

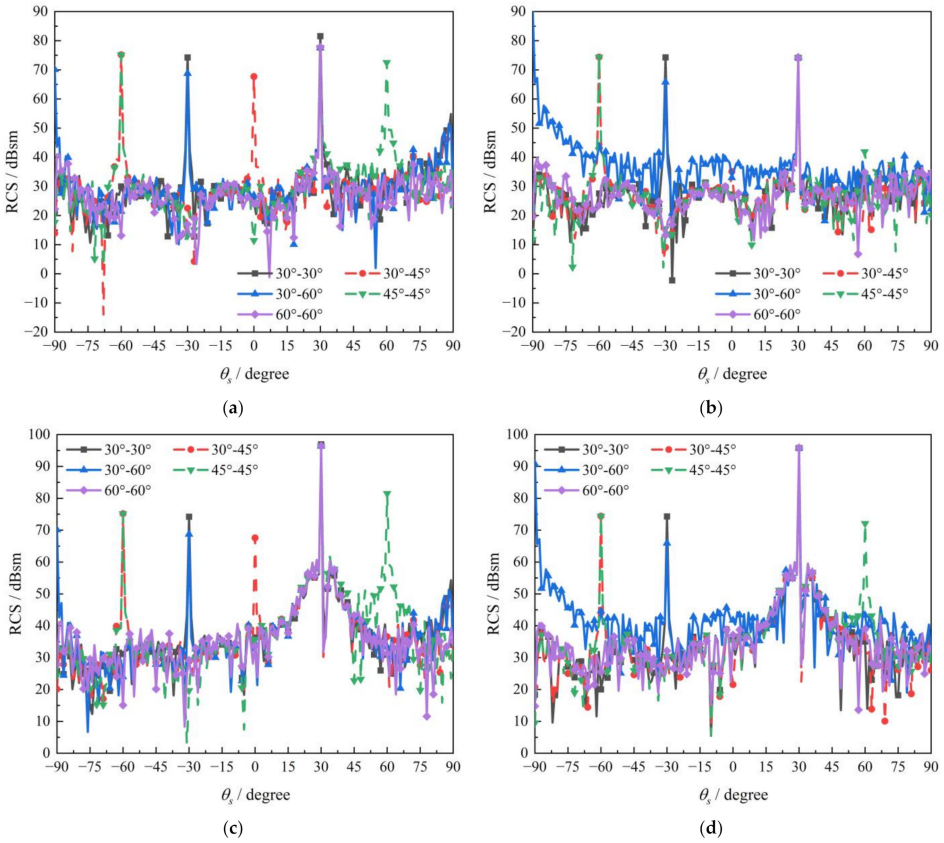


Figure 15. Bistatic RCS simulation results: (**a**) canyon, HH-polarization; (**b**) canyon, VV-polarization; (**c**) valley, HH-polarization; (**d**) valley, VV-polarization.

Similarly, when the slope angles are $30° - 45°$, the peak at $\theta_s = 0°$ disappears in VV polarization. The reason is that when the incident angle is equal to the Brewster angle of the environment, the reflection wave will be fragile, and even disappear. The Brewster angle of the terrestrial in this paper is 60° [42]. Note the path marked by yellow in Figure 14d. The incident wave hit the left slope and reflected to the bottom; as the incident angle is 60°, because of the Brewster effect the reflection wave from the bottom is weak, as a result, the peak at $\theta_s = 60°$ disappears. Then, as shown in Figure 14b, when the incident wave hit the left slope at the Brewster angle, the reflection wave decreased sharply, leading to the scattering wave at $\theta_s = 0°$ disappearing. It is worth noting that the curves of the combinations of $45° - 45°$, in Figure 15b,d, have different performances at $\theta_s = 60°$, even though they are both in VV polarization. The difference of the bottom can explain the phenomenon. The Brewster angle for the water bottom is about 80°, while the incident angle is 60°, so the reflection marked by the yellow of the valley bottom is still strong and makes the peak at $\theta_s = 60°$ apparent. Hence, the structure of the canyon/valley environment decides the peak position; the surface type affects the peak values; Brewster effect produces special points.

Table 2. Peak values of different slope-angle combinations.

Figures	Slope Angles	Peak Angles	Peak Value (dBsm)
(**a**)	30°–30°	−30°, 30°	(74.2635, 81.5739)
	30°–45°	−60°, 0°, 30°	(75.1674, 67.6920, 77.5633)
	30°–60°	−90°, −30°, 30°	(70.1196, 68.7718, 77.5377)
	45°–45°	−60°, 30°, 60°	(75.1537, 77.6434, 72.5114)
	60°–60°	30°	(77.8450)
(**b**)	30°–30°	−30°, 30°	(74.2758, 74.1240)
	30°–45°	−60°, 0°, 30°	(74.3754, 35.1071, 74.1474)
	30°–60°	−90°, −30°, 30°	(90.7841, 65.8235, 74.1959)
	45°–45°	−60°, 30°, 60°	(74.3739, 74.1578, 41.8799)
	60°–60°	30°	(73.9862)
(**c**)	30°–30°	−30°, 30°	(74.2336, 96.9393)
	30°–45°	−60°, 0°, 30°	(75.1781, 67.5802, 96.3810)
	30°–60°	−90°, −30°, 30°	(70.0889, 68.7210, 96.3766)
	45°–45°	−60°, 30°, 60°	(75.1604, 96.4070, 81.4939)
	60°–60°	30°	(96.4129)
(**d**)	30°–30°	−30°, 30°	(74.3121, 95.7886)
	30°–45°	−60°, 30°	(74.3823, 95.7901)
	30°–60°	−90°, −30°, 30°	(90.7844, 65.9220, 95.7933)
	45°–45°	−60°, 30°, 60°	(74.3808, 95.7944, 72.1102)
	60°–60°	30°	(95.7745)

4.5. Composite Scattering of Canyon/Valley Composite Rough Surface with Different Surface Roughness

In this subsection, the bistatic composite scattering characteristics of the canyon and valley environment with different roughness are investigated. The slope angle $\alpha_1 = 30°$, $\alpha_3 = 30°$, the RMS height h_{rms} and the wind speed $v_{19.5}$ are as shown in Figure 16. The incident angle is $(\theta_i, \varphi_i) = (-30°, 90°)$, and the observation angles are $(\theta_s, \varphi_s) = (-90° \sim 90°, 90°)$. The illustration of simulation geometry is the same as Section 4.3, which is shown in Figure 12. Numerical results are shown in Figure 16; the specific peak values are listed in Table 3 in the order of black, red, blue, green and purple curves.

As shown in Figure 16 and Table 3, the roughness of the canyon/valley environment mainly affects the peak values. Take Figure 16a as an example. Comparing the black curve and red curve, when the roughness of the bottom increases from 0.2λ to 0.5λ, while the roughness of the slopes remains unchanged, the peak values at $\theta_s = 30°$ decrease from 81.5529 dBsm to 76.6757 dBsm, while the peak values at $\theta_s = -30°$ remain nearly constant. The reason could be that with the increase in bottom surface roughness, the specular reflection of the bottom gets weaker. Referring to the analysis in Section 4.2 and 4.3, the specular reflection characteristic of the bottom decides the peak values at $\theta_s = 30°$. As a result, the peak values at $\theta_s = 30°$ decrease. We can draw the same conclusion by comparing the green and purple curves.

Table 3. Peak values of different roughness combinations.

Figures	Peak Angles	Peak Value (dBsm)
(**a**)	−30°	(74.2836, 74.2807, 74.2795, 59.0459, 59.0324)
	30°	(81.5529, 76.3757, 80.3007, 79.3965, 71.7860)
(**b**)	−30°	(74.2719, 74.2705, 74.2716, 58.9953, 58.9857)
	30°	(74.0700, 62.5396, 74.0811, 74.0906, 62.6144)
(**c**)	−30°	(74.3136, 74.3083, 74.3019, 59.1785, 59.1405)
	30°	(96.9244, 95.3232, 96.7281, 96.5997, 94.9308)
(**d**)	−30°	(74.2984, 74.2920, 74.2971, 59.1511, 59.1155)
	30°	(95.7729, 94.0520, 95.7739, 95.7748, 94.0543)

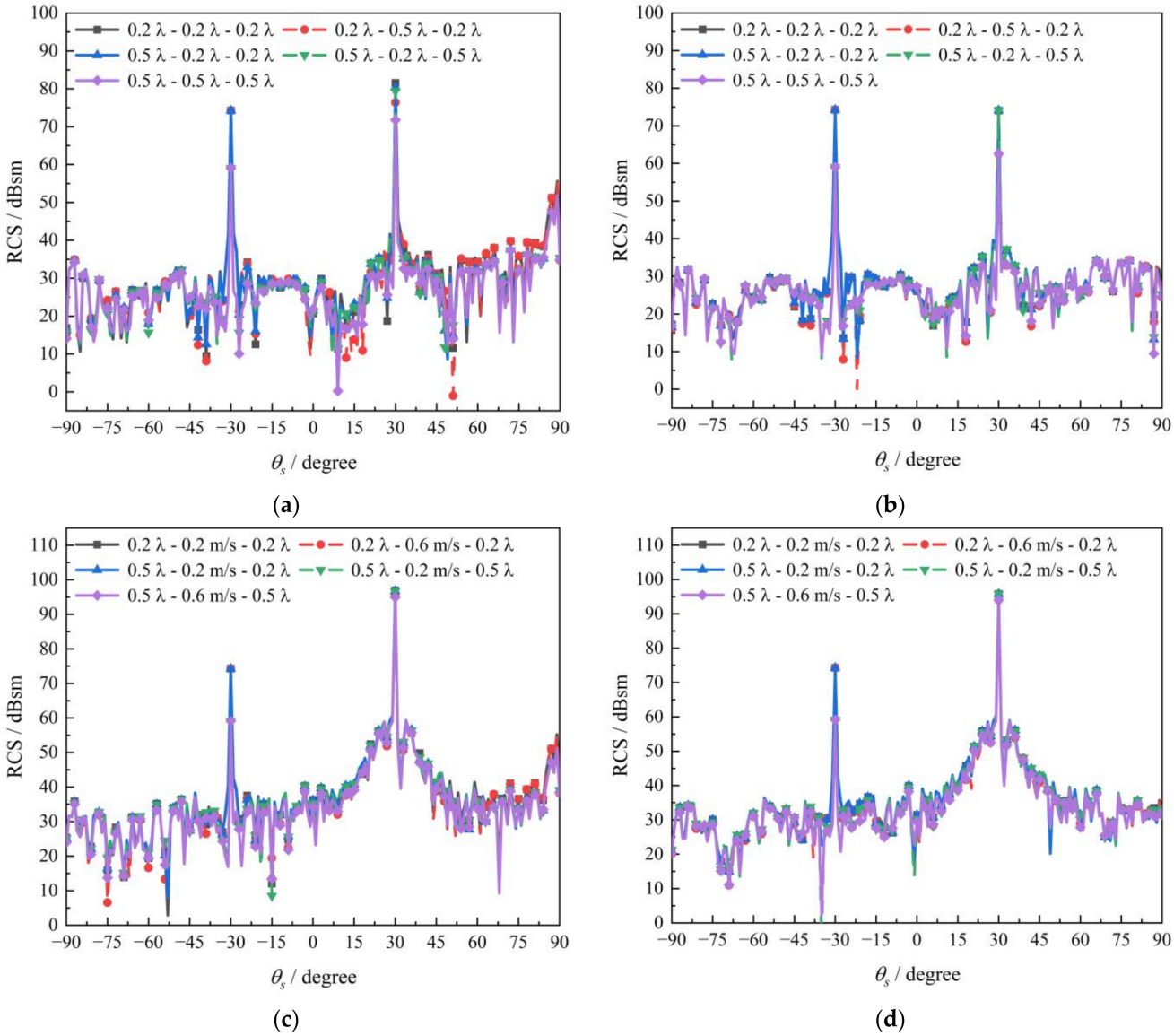


Figure 16. Bistatic RCS simulation results: (**a**) canyon, HH-polarization; (**b**) canyon, VV-polarization; (**c**) valley, HH-polarization; (**d**) valley, VV-polarization.

Similarly, the peak values at $\theta_s = -30^\circ$ are mainly affected by the roughness of the right slope. Comparing the blue curve and green curve, when the roughness of the right slope increases from 0.2λ to 0.5λ, while the roughness of the left slopes and the bottom remains unchanged, the peak value at $\theta_s = -30^\circ$ decreases from 74.2975 dBsm to 59.0459 dBsm, while the peak values at $\theta_s = 30^\circ$ change less 1 dBsm.

The above analysis is still valid for Figure 16b to Figure 16d. Now, we can conclude that the roughness variations of the bottom will mainly affect the forward scattering peak values, while the slopes affect another group. The roughness increases and the peak values decrease. The conclusion is of great significance for environmental parameter inversion.

4.6. Composite Scattering of Canyon/Valley Environment with Different Incident Azimuth Angles

This subsection investigates the monostatic composite scattering characteristics of canyon and valley environments with different incident azimuth angles. The RMS height $h_{\text{rms}} = 0.2\lambda$, the wind speed $v_{19.5} = 0.2$ m/s, and the slope angles $\alpha_1 = 30^\circ$, $\alpha_3 = 45^\circ$. The incident pitch angles are 30°, 45°, 60° respectively, the incident azimuth angles are $0^\circ \sim 360^\circ$. The illustration of simulation geometry is shown in Figure 17.

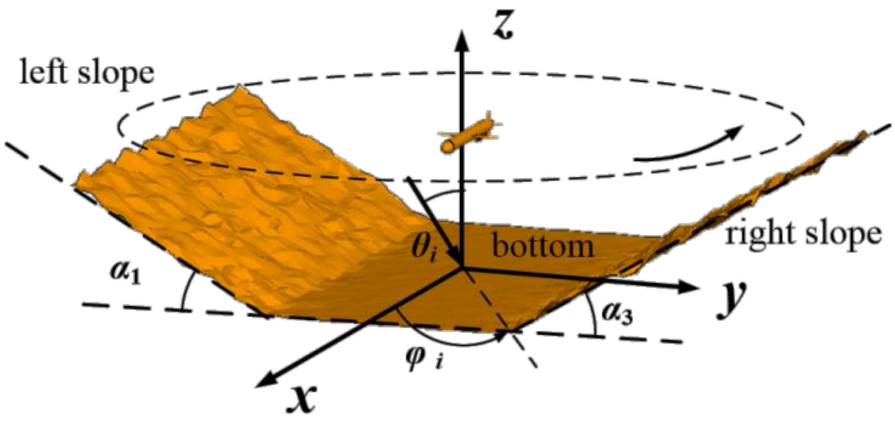


Figure 17. The geometry of a missile-like target above composite rough surface for monostatic scattering.

As shown in Figure 18a, each curve has two significant peaks located at $\varphi_s = 90^\circ$ and $\varphi_s = 270^\circ$, respectively. When the incident pitch angle is 30°, the highest peak value occurs at $\varphi_s = 90^\circ$, where the incident wave hits the left slopes vertically and reflects vertically. Observing the red curve, the incident pitch angle is 45°, and the highest peak value appears at $\varphi_s = 270^\circ$, where the incident wave and reflection field are vertical to the right slope. As for the blue curve, when the incident pitch angle is 60°, though the peak values are not the highest in the three curves, the values are still much higher than the values at other azimuth angles. This phenomenon can be attributed to the multiple bouncing when the incident planes are vertical to the slopes, which may raise the power distribution in the opposite direction of the incident. When the incident azimuth angles are any angles rather than 90° and 270°, we can barely find an angle whose value dominates over those of other angles. The semi-enclosed cavity structure makes the power redistribute, and the target is harder to be detected. What's more, when we detect a target flying above the canyon or valley environment, it is better to avoid the side view directions. Similar analyses can be concluded from Figure 18b to Figure 18d.

4.7. Composite Scattering of Canyon/Valley Environment with or without Target

In this subsection, the monostatic composite scattering characteristics of one target or none above the canyon environment are investigated. The RMS height $h_{\text{rms}} = 0.2\lambda$, the slope angles $\alpha_1 = 30^\circ$, $\alpha_3 = 45^\circ$. The incident angles are $(\theta_i, \varphi_i) = (-90^\circ \sim 90^\circ, 90^\circ)$. The illustration of simulation geometry is shown in Figure 19.

As shown in Figure 20, each curve has three peaks at $\theta_s = -45^\circ$, $\theta_s = 0^\circ$, $\theta_s = 30^\circ$, respectively. The main reason the peaks appear in these three angles is the structure of the canyon. When incident waves hit the slope or the bottom vertically, the peak appears, which means the vertical reflection field from the environment dominates the scattering field. What's more, comparing the black/red curve and the blue/green curve, we can draw out that the target scattering fields play a more critical role when the incident waves hit the slopes or bottom non-vertically than vertically.

This discipline is also suitable for Figure 20b, which displays the results for a valley model with wind speed $v_{19.5} = 0.2$ m/s. Additionally, the peak value at $\theta_s = 0^\circ$ in Figure 20b is much higher than in Figure 20a, because the calm water can reflect more power vertically than the rough terrestrial bottom.

These results enlighten us that when we detect the targets above the canyon/valley environment, the incident EM waves should best not illuminate the slopes or bottom vertically.

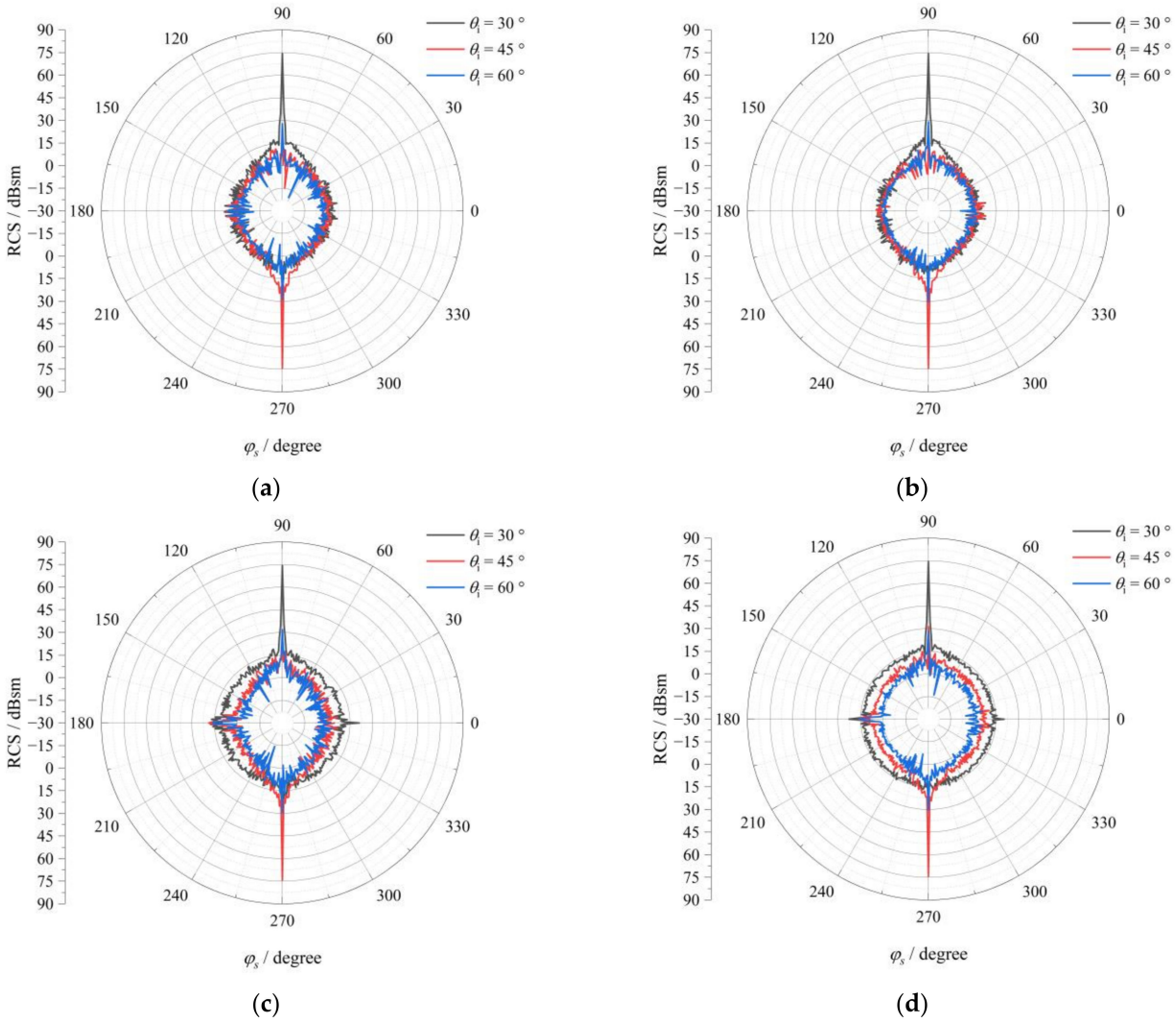


Figure 18. Monostatic RCS simulation results: (**a**) canyon, HH-polarization; (**b**) canyon, VV-polarization; (**c**) valley, HH-polarization; (**d**) valley, VV-polarization.

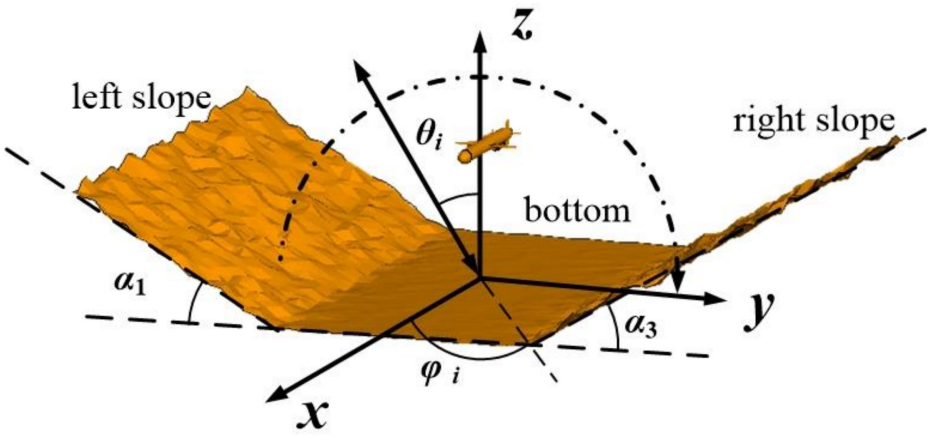


Figure 19. The geometry of a missile-like target above composite rough surface for monostatic scattering.

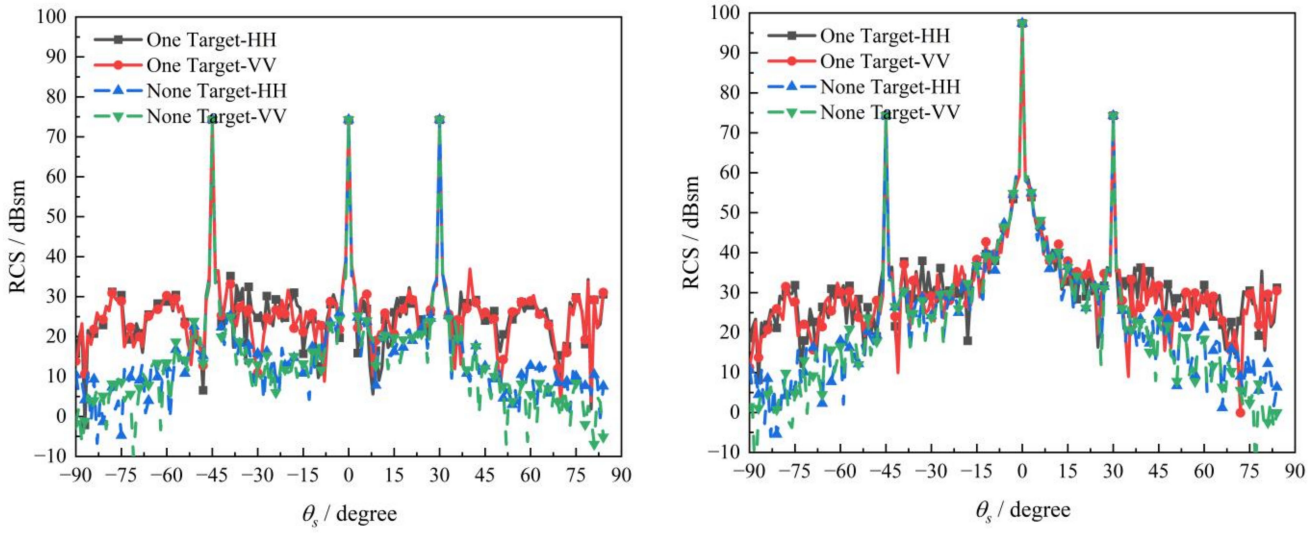


Figure 20. Monostatic RCS simulation results: (**a**) canyon composite rough surface; (**b**) valley composite rough surface.

4.8. Composite Scattering of Canyon/Valley Environment with Different Incident Angles

This example investigates the bistatic composite scattering characteristics of the canyon and valley environment with different incident angles. The slope angle $\alpha_1 = 30°$, $\alpha_3 = 30°$, the RMS height $h_{\text{rms}} = 0.2\lambda$, and the wind speed $v_{19.5} = 0.2$ m/s. The incident pitch angles are $-30°$, $-45°$, $-60°$ respectively, while $\varphi_i = 90$, the observation angles are $(\theta_s, \varphi_s) = (-90° \sim 90°, 90°)$. The illustration of simulation geometry is the same as Section 4.3, which is shown in Figure 12.

As shown in Figure 21, each curve has two peaks. One of the peaks is produced by the reflection of the incident wave from the bottom of the canyon/valley environment. The other one results from the multiple bounces of the EM waves in the semi-enclosed cavity structure. The main paths are shown in Figure 22. Please pay attention to Figure 21b; geometrically, there should be three peaks when the incident angle is 45°; however, there are actually only two peaks, $\theta_s = -15°$ and $\theta_s = 45°$. The reason may be that the paths marked by yellow reflect three times, and the scattering field decreases quickly after each reflection so that when the wave leaves the composite rough surface, the field is too weak to be recognized. Based on the results, the incident angle also decides the peak position. Though multiple bounces exist in the canyon/valley environment, the higher-order bounce is usually weak enough to ignore.

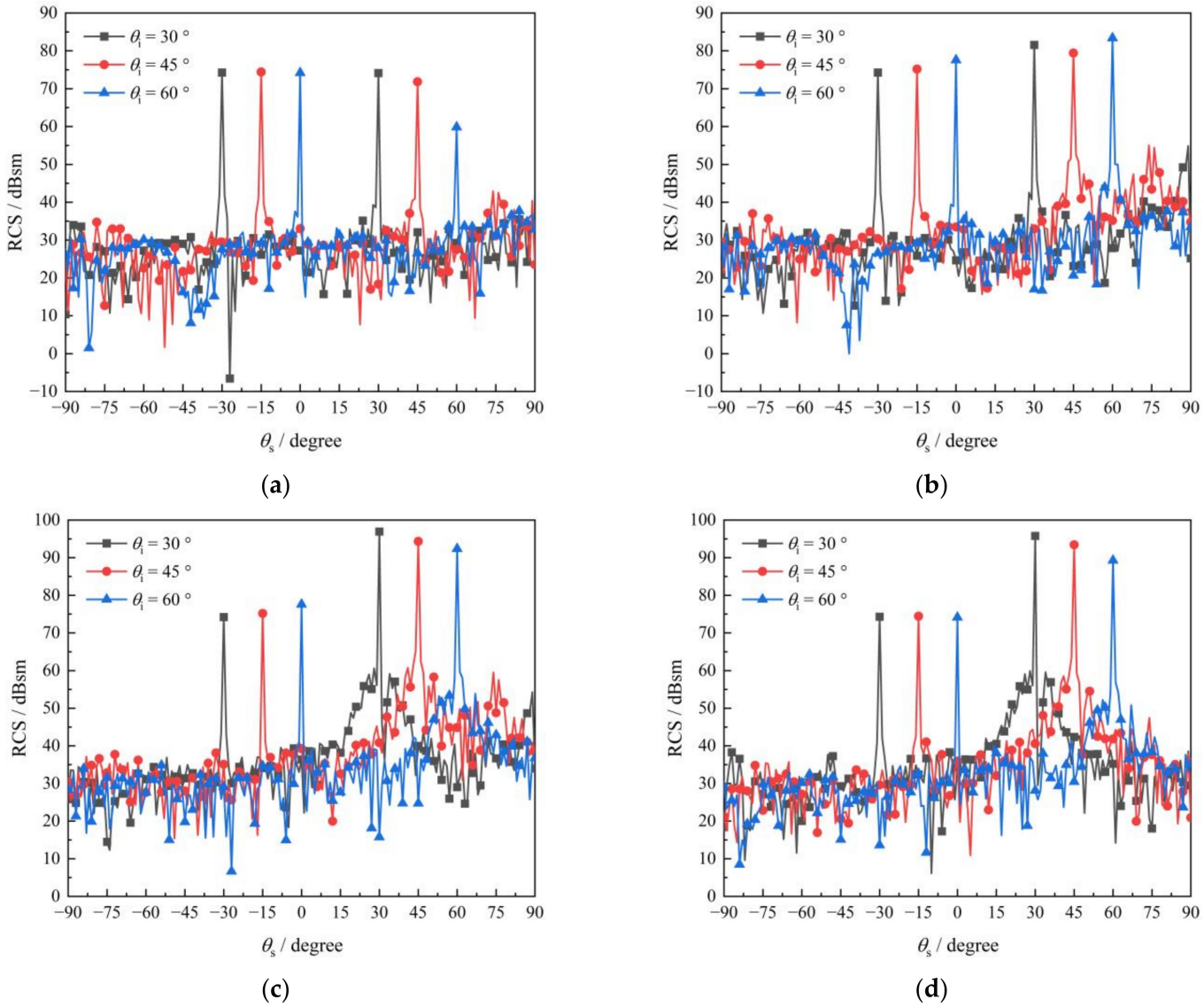


Figure 21. Bistatic RCS simulation results: (**a**) canyon, HH-polarization; (**b**) canyon, VV-polarization; (**c**) valley, HH-polarization; (**d**) valley, VV-polarization.

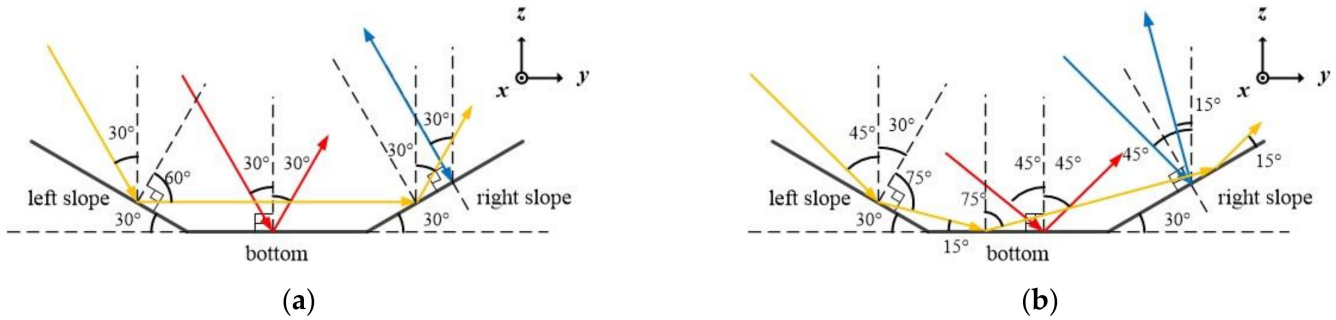
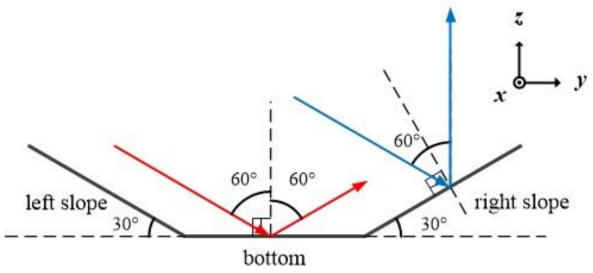


Figure 22. *Cont.*



(**c**)

Figure 22. Illustration of EM wave propagation paths in canyon/valley: (**a**) $\theta_i = -30°$; (**b**) $\theta_i = -45°$; (**c**) $\alpha_i = -60°$.

5. Conclusions

In this article, a method based on composite surface modeling theory is put forward to establish the typical canyon/valley environment containing two slopes and a plain bottom which forms the semi-enclosed cavity structure. Then modified SBR algorithm improved by introducing a high-order reflection model is proposed. Facet-based SSA method is investigated and integrated with the modified SBR algorithm to solve the composite scattering from a target above the canyon/valley environment efficiently and accurately. The composite EM scattering characteristics influenced by surface types and roughness, slope angles, incident pitch, and azimuth angles are thoroughly analyzed. It can be concluded that: the incident angle and the slope angle determine the peak numbers and positions of the RCS curves; the roughness and Brewster Effect affect the peak values; and the target above the composite surface, and the particular structure of the canyon/valley, make the multi-bounce scattering mechanism more complicated. The work presented in this article has significance for detecting targets in the canyon/valley environment.

However, there are some limitations in the articles and future work will focus on two aspects. Firstly, in our canyon/valley model, the Gauss and PM surfaces are still approximations. If the real geometry data for the canyon/valley environment surface can be obtained, it will make the modeling more practical. Secondly, the EM scattering simulation results for a target above the canyon/valley environment are compared with the accurate numerical algorithm results, instead of the measured data. Due to the absence of the measured data from the public literature or experimental results, we would like to carry out some experiments to obtain the real composite EM scattering characteristics, which can be used to justify and correct our model.

Author Contributions: Conceptualization, Y.W. and T.W.; methodology, Y.W. and T.W.; software, Y.W.; validation, T.W.; writing—original draft preparation, Y.W. and T.W.; writing—review and editing, X.L., Q.W. and Z.W.; supervision, C.T. All authors have read and agreed to the published version of the manuscript.

Funding: This research was funded by the National Natural Science Founding of China, grant number 62201611, and the Natural Science Foundation of Shaanxi Province, grant number 2021JQ-365.

Institutional Review Board Statement: Not applicable.

Informed Consent Statement: Not applicable.

Data Availability Statement: All data generated or analyzed during this study are included in this published article.

Conflicts of Interest: The authors declare no conflict of interest.

References

1. Liu, Z.; Wang, C. Physics-Based Automatic Recognition of Small Features Located in Highly Similar Structures with Electromagnetic Scattering Data. *IEEE J. Multiscale Multiphysics Comput. Tech.* **2022**, *7*, 312–319. [CrossRef]
2. Idriss, Z.; Raj, R.G.; Narayanan, R.M. A Computational Electromagnetics and Sparsity-Based Feature Extraction Approach to Ground-Penetrating Radar Imaging. *IEEE Trans. Geosci. Remote Sens.* **2022**, *60*, 1–15. [CrossRef]
3. Zhang, L.; Chen, Y.; Wang, N.; Zou, B.; Liu, S. Scattering Mechanism Analysis of Man-Made Targets via Polarimetric SAR Observation Simulation. *IEEE J. Sel. Top. Appl. Earth Observ. Remote Sens.* **2022**, *15*, 919–929. [CrossRef]
4. Tsang, L.; Liao, T.; Tan, S.; Huang, H.; Qiao, T.; Ding, K. Rough Surface and Volume Scattering of Soil Surfaces, Ocean Surfaces, Snow, and Vegetation Based on Numerical Maxwell Model of 3-D Simulations. *IEEE J. Sel. Top. Appl. Earth Observ. Remote Sens.* **2017**, *10*, 4703–4720. [CrossRef]
5. Tsang, L.; Liao, T.; Gao, R.; Xu, H.; Gu, W.; Zhu, J. Theory of Microwave Remote Sensing of Vegetation Effects, SoOp and Rough Soil Surface Backscattering. *Remote Sens.* **2022**, *14*, 3640. [CrossRef]
6. Yao, H.; Zhang, Y.; Jiang, L.; Ewe, H.T.; Ng, M. Snow Parameters Inversion from Passive Microwave Remote Sensing Measurements by Deep Convolutional Neural Networks. *Sensors* **2022**, *22*, 4769. [CrossRef]
7. Dai, L.; Che, T.; Xiao, L.; Akynbekkyzy, M.; Zhao, K.; Leppanen, L. Improving the Snow Volume Scattering Algorithm in a Microwave Forward Model by Using Ground-Based Remote Sensing Snow Observations. *IEEE Trans. Geosci. Remote Sens.* **2022**, *60*, 1–17. [CrossRef]
8. Liu, H.; Chen, Z.; Zhao, C. A New Doppler Model Incorporated with Free and Broken-Short Waves for Coherent S-Band Wave Radar at Near-Grazing Angles. *IEEE Trans. Geosci. Remote Sens.* **2022**, *60*, 1–11. [CrossRef]
9. Jiang, W.; Zhang, M.; Nie, D.; Sun, R. Ship Motion Estimation from Polarized Doppler Spectra from Ship Wakes on Two-Dimensional Sea Surfaces. *Waves Random Complex Media* **2016**, *26*, 284–300. [CrossRef]
10. Jia, C.; Guo, L.; Yang, P. EM Scattering from a Target Above a 1-D Randomly Rough Sea Surface Using GPU-Based Parallel FDTD. *IEEE Antennas Wirel. Propag. Lett.* **2015**, *14*, 217–220. [CrossRef]
11. Li, J.; Guo, L.X.; Zeng, H. FDTD Investigation on Electromagnetic Scattering from Two-Layered Rough Surfaces under UPML Absorbing Condition. *Chin. Phys. Lett.* **2009**, *26*, 034101.
12. Li, J.; Guo, L.X.; Zeng, H. FDTD Investigation on Bistatic Scattering from Two-Dimensional Rough Surface with UPML Absorbing Condition. *Waves Random Complex Media* **2009**, *19*, 418–429. [CrossRef]
13. Yang, X.; Jiang, M.; Shen, L.; Jia, P.; Rong, Z.; Chen, Y.; Lei, L.; Hu, J. A Flexible FEM-BEM-DDM for EM Scattering by Multiscale Anisotropic Objects. *IEEE Trans. Antennas Propag.* **2021**, *69*, 8562–8573. [CrossRef]
14. Johnson, J.T. A Study of the Four-Path Model for Scattering from an Object above a Half Space. *Microw. Opt. Technol. Lett.* **2001**, *30*, 130–134. [CrossRef]
15. Wang, Y.; Tong, C. A Novel Method of Suppressing Multipath Interference Based on Brewster Effect. In Proceedings of the Eleventh International Conference on Signal Processing Systems, Chengdu, China, 15–17 November 2019; Mao, K., Ed.; SPIE: Bellingham, WA, USA, 2019; Volume 11384.
16. Zou, G.X.; Tong, C.M.; Sun, H.L.; Peng, P.; Song, T. Brewster Effect of Super-Low Altitude Target above Terrestrial Environments using Modified Facet-based Weighted Four-Path Model. *Int. J. RF Microw. Comput. Aided Eng.* **2021**, *31*, e22564. [CrossRef]
17. Ling, H.; Chou, R.C.; Lee, S.W. Shooting and Bouncing Rays—Calculating the RCS of an Arbitrarily Shaped Cavity. *IEEE Trans. Antennas Propag.* **1989**, *37*, 194–205. [CrossRef]
18. Fan, T.; Guo, L.; Liu, W. A Novel OpenGL-Based MoM/SBR Hybrid Method for Radiation Pattern Analysis of an Antenna Above an Electrically Large Complicated Platform. *IEEE Trans. Antennas Propag.* **2016**, *64*, 201–209. [CrossRef]
19. Dong, C.L.; Guo, L.X.; Meng, X.; Wang, Y. An Accelerated SBR for EM Scattering from the Electrically Large Complex Objects. *IEEE Antennas Wirel. Propag. Lett.* **2018**, *17*, 2294–2298. [CrossRef]
20. Huang, Y.; Zhao, Z.Q.; Ql, C.H.; Nie, Z.P.; Liu, Q.H. Fast Point-Based KD-Tree Construction Method for Hybrid High Frequency Method in Electromagnetic Scattering. *IEEE Access* **2018**, *6*, 38348–38355. [CrossRef]
21. Guo, G.B.; Guo, L.X. SBR Methods for Near-Field Scattering of an Electrically Large Complex Target Illuminated by Dipole Sources. *IEEE Access* **2018**, *6*, 78710–78718. [CrossRef]
22. Guo, G.B.; Guo, L.X.; Wang, R. The Study on Near-Field Scattering of a Target Under Antenna Irradiation by TDSBR Method. *IEEE Access* **2019**, *7*, 113476–113487. [CrossRef]
23. Guo, G.B.; Guo, L.X. Hybrid Time-Domain PTD and Physical Optics Contour Integral Representations for the Near-Field Backscattering Problem. *IEEE Trans. Antennas Propag.* **2019**, *67*, 2655–2665. [CrossRef]
24. Wang, J.J.; Guo, L.X.; Wei, Y.W.; Chai, S.R. Application of the Improved SBR-TSM Based on MPI to EM Scattering from Multiple Targets Above a 3-D Rough Sea Surface. *IEEE Antennas Wirel. Propag. Lett.* **2022**, *21*, 411–415. [CrossRef]
25. Sun, H.L.; Tong, C.M.; Zou, G.X. High Efficiency Iterative Solver for Modeling Composite Rough Surface Electromagnetic Scattering. *Electromagnetics* **2017**, *37*, 113–126. [CrossRef]
26. Zou, G.X.; Tong, C.; Sun, H.L.; Wang, T.; Tian, G.L. Modeling and Electromagnetic Scattering of Composite Rough Surface of Island in Deep Sea. In Proceedings of the 2017 International Applied Computational Electromagnetics Society Symposium (ACES), Suzhou, China, 1–4 August 2017; pp. 1–2.
27. Zou, G.X.; Tong, C.M.; Sun, H.L.; Peng, P. Research on Electromagnetic Scattering Characteristics of Combined Conducting and Dielectric Target Above Coastal Environment. *IEEE Access* **2020**, *8*, 169286–169303. [CrossRef]

28. Zou, G.X.; Tong, C.M.; Sun, H.L.; Wang, T.; Peng, P. A Hybrid Method for Electromagnetic Scattering from Target above Composite Rough Surface of Ground and Near Sea in Adjacent Region. *Electromagnetics* **2018**, *38*, 415–437. [CrossRef]
29. Chai, S.; Li, H.; Li, J. Simulation of Radar Scattering Characteristics of A Target Located in Ground-Sea Junction Area Based on Improved SBR Algorithm. In Proceedings of the 2020 Cross Strait Radio Science & Wireless Technology Conference (CSRSWTC), Fuzhou, China, 13–16 December 2020; pp. 1–3.
30. Zou, G.X.; Tong, C.M.; Zhu, J.; Sun, H.L.; Peng, P. Study on Composite Electromagnetic Scattering Characteristics of Low-Altitude Target Above Valley Composite Rough Surface Using Hybrid SBR-EEC Method. *IEEE Access* **2020**, *8*, 72298–72307. [CrossRef]
31. Wang, Z.L.; Tong, C.M.; Wang, Y.J.; Wang, Q.K.; Zou, G.X. Study on Environment Modeling and Electromagnetic Scattering Characteristics in Mountainous Areas. *Electromagnetics* **2022**, *42*, 192–209. [CrossRef]
32. Brown, G.S. Backscattering from a Gaussian-Distributed Perfectly Conducting Rough Surface. *IEEE Trans. Antennas Propag.* **1978**, *26*, 472–482, Correction in *IEEE Trans. Antennas Propag.* **1980**, *28*, 943–946. [CrossRef]
33. Pierson, W.J.; Moskowitz, L. A Proposed Spectral Form for Fully Developed Wind Seas based on the Similarity Theory of SA Kitaigorodskii. *J. Geophys. Res.* **1964**, *69*, 5181–5190. [CrossRef]
34. Maoguang, W. *Theory of Geometric Diffraction*, 2nd ed.; Xidian Universitiy Press: Xi'an, China, 1994.
35. Deroo, R.D.; Ulaby, F.T. Bistatic Specular Scattering from Rough Dielectric Surfaces. *IEEE Trans. Antennas Propag.* **1994**, *42*, 220–231. [CrossRef]
36. Beard, C.I. Coherent and Incoherent Scattering of Microwaves from the Ocean. *IEEE Trans. Antennas Propag.* **1961**, *9*, 470–483. [CrossRef]
37. Gordon, W.B. High-Frequency Approximations to the Physical Optics Scattering Integral. *IEEE Trans. Antennas Propag.* **1994**, *42*, 427–432. [CrossRef]
38. Michaeli, A. Equivalent Edge Currents for Arbitrary Aspects of Observation. *IEEE Trans. Antennas Propag.* **1984**, *32*, 252–258. [CrossRef]
39. Voronovich, A.G.; Zavorotny, V.U. The Transition from Weak to Strong Diffuse Radar Bistatic Scattering From Rough Ocean Surface. *IEEE Trans. Antennas Propag.* **2017**, *65*, 6029–6034. [CrossRef]
40. Voronovich, A.G.; Zavorotny, V.U. Theoretical Model for Scattering of Radar Signals in Ku- and C-bands from a Rough Sea Surface with Breaking Waves. *Waves Random Media* **2001**, *11*, 247–269. [CrossRef]
41. Elfouhaily, T.M.; Guerin, C.A. A Critical Survey of Approximate Scattering Wave Theories from Random Rough Surfaces. *Waves Random Media* **2004**, *14*, R1–R40. [CrossRef]
42. Lixin, G.; Min, Z.; Zhensen, W. *Basic Theory and Method of Composite Electromagnetic Scattering from Random Rough Surface and Target*; Science Press: Beijing, China, 2014.
43. Hallikainen, M.T.; Ulaby, F.T.; Dobson, M.C.; Elrayes, M.A.; Wu, L.K. Microwave Dielectric Behavior of Wet Soil-Part 1. Empricial-Models and Expremental-Observations. *IEEE Trans. Geosci. Remote Sens.* **1985**, *23*, 25–34. [CrossRef]
44. Dobson, M.C.; Ulaby, F.T.; Hallikainen, M.T.; Elrayes, M.A. Microwave Dielectric Behavior of Wet Soil-Part 2. Dielectric Mixing Models. *IEEE Trans. Geosci. Remote Sens.* **1985**, *23*, 35–46. [CrossRef]

Disclaimer/Publisher's Note: The statements, opinions and data contained in all publications are solely those of the individual author(s) and contributor(s) and not of MDPI and/or the editor(s). MDPI and/or the editor(s) disclaim responsibility for any injury to people or property resulting from any ideas, methods, instructions or products referred to in the content.